SANDIA REPORT
SAND2020-9893
Printed September 2020

Sandia National Laboratories

Advancing the science of explosive fragmentation and afterburn fireballs though experiments and simulations at the benchtop scale

Daniel R. Guildenbecher, Ann R. Dallman, Elise M. Hall, Benjamin R. Halls, Elizabeth M.C. Jones, Sean P. Kearney, Ryan T. Marinis, Christopher Murzyn, Daniel R. Richardson, Francisco Perez, Phillip L. Reu, Andrew D. Thompson, Marc C. Welliver
Sandia National Laboratories
Albuquerque, New Mexico

Ellen Chen Mazumdar
Georgia Institute of Technology
Atlanta, Georgia

Timothee L. Pourpoint, Catriona M.L. White, Alex D. Brown
Purdue University
West Lafayette, Indiana

S. Balachandar, Ryan W. Houim
University of Florida
Gainesville, Florida

Prepared by
Sandia National Laboratories
Albuquerque, New Mexico
87185 and Livermore,
California 94550

Issued by Sandia National Laboratories, operated for the United States Department of Energy by National Technology & Engineering Solutions of Sandia, LLC.

Available to DOE and DOE contractors from
U.S. Department of Energy
Office of Scientific and Technical Information
P.O. Box 62
Oak Ridge, TN 37831

Telephone: (865) 576-8401
Facsimile: (865) 576-5728
E-Mail: reports@osti.gov
Online ordering: http://www.osti.gov/scitech

Available to the public from
U.S. Department of Commerce
National Technical Information Service
5301 Shawnee Rd
Alexandria, VA 22312

Telephone: (800) 553-6847
Facsimile: (703) 605-6900
E-Mail: orders@ntis.gov
Online order: https://classic.ntis.gov/help/order-methods/

ABSTRACT

Detonation of explosive devices produces extremely hazardous fragments and hot, luminous fireballs. Prior experimental investigations of these post-detonation environments have primarily considered devices containing hundreds of grams of explosives. While relevant to many applications, such large-scale testing also significantly restricts experimental diagnostics and provides limited data for model validation. As an alternative, the current work proposes experiments and simulations of the fragmentation and fireballs from commercial detonators with less than a gram of high explosive. As demonstrated here, reduced experimental hazards and increased optical access significantly expand the viability of advanced imaging and laser diagnostics. Notable developments include the first known validation of MHz-rate optical fragment tracking and the first ever Coherent Anti-Stokes Raman Scattering (CARS) measures of post-detonation fireball temperatures. While certainly not replacing the need for full-scale verification testing, this work demonstrates new opportunities to accelerate developments of diagnostics and predictive models of post-detonation environments.

ACKNOWLEDGEMENTS

Efforts discussed here were inspired by the late Senior Scientist, Steve Attaway. Steve's scientific vision and passion for national security missions inspired us all. We are forever grateful for his guidance and mentorship.

The authors would like to thank the many individuals at Sandia National Laboratories who supported this effort. Experiments would not have been possible without the dedicated support of Paul Farias, Thomas Grasser, James Patrick Ball, Howard Lee Stauffacher, Sam Reardon, Glenn White, and Luke Lebow. Additional technical support was provided by Tim Miller, Megan Paciaroni, and many others. Finally, we gratefully acknowledge the support of the Laboratory Directed Research and Development (LDRD) program at Sandia National Laboratories.

CONTENTS

LIST OF FIGURES

ACRONYMS AND DEFINITIONS

Abbreviation	Definition
AMR	Adaptive Mesh Refinement
CARS	Coherent Anti-Stokes Raman Scattering
CFD	Computational Fluid Dynamics
DIC	Digital Image Correlation
EBW	Exploding Bridgewire
EDS	Energy Dispersive X-ray Spectroscopy
EOS	Equation of State
FOV	Field of View
LDRD	Laboratory Directed Research and Development
LES	Large Eddy Simulation
LII	Laser Induced Incandescence
PBX	Plastic Bonded Explosive
PDV	Photonic Doppler Velocimetry
PETN	Pentaerythritol Tetranitrate
RDX	Royal Demolition Explosive
SEM	Scanning Electron Microscopy

1. INTRODUCTION AND MOTIVATION

The detonation of explosives produces complex and harsh environments [1]. Strong shock waves lead to pressure loading that can damage surrounding objects. If energetics are enclosed within a structural case, fragments may also be generated. These fragments propagate outward with velocities on the order of kilometers per second, adding significant hazards. Furthermore, the products of detonation may mix with the surrounding air and oxidize to produce hot, turbulent, and luminous afterburn fireballs. Accurate predictions of these post-detonation environments are needed for numerous industrial and military applications, including ordnance design, safety analysis, forensics, etc. This has motivated development of numerical methods for three-dimensional (3D) and time-resolved simulations, including recent literature examples predicting case fragmentation [2-9] and fireball combustion [10-16].

To identify gaps in current simulation capabilities and advance predictive models, detailed experimental validation datasets are needed. An ideal experiment would quantify all relevant phenomena predicted by simulations, including initiation of the high-explosive, internal propagation of detonation waves, case pressurization, fragmentation, release of gas-phase shock waves, post-detonation chemistry, mixing with the surrounding environment, and combustion. In addition, experiments should be repeated many times to quantify shot-to-shot statistical variations and should be reproducible by others. Unfortunately, due to extreme hazards and optically opaque environments, many of these phenomena are difficult to measure, especially in outdoor test arenas. Furthermore, due to costs, most literature results provide limited experimental repetitions. Finally, much of the prior literature considers unique geometries, complicating end-to-end model validation.

Motivated by these challenges, the current report summarizes progress achieved during a 2018-2020 Laboratory Directed Research and Development (LDRD) effort at Sandia National Laboratories. The main goals of this effort were:

1. Advance experimental methods for quantification of post-detonation phenomena, especially case fragmentation and fireball combustion.
2. Develop a validation quality experimental dataset, quantifying as much of the relevant phenomena as possible, using an experimental geometry that enables repetition and is reproducible by others.
3. Demonstrate a pathway to apply the experimental results for improved validation of computational simulations.

A central hypothesis of the current work is that the above goals can be achieved with small-scale experimental devices containing less than a gram of high explosive. As demonstrated throughout the rest of this report, these small-scale devices have reduced hazards, are significantly less optically opaque, and are orders-of-magnitude less expensive compared to many application-specific, full-scale devices. Of course, reducing device sizes, as proposed here, may lead to complex and perhaps poorly understood physical scaling of the coupled multi-phase and multi-physics phenomena governing the behavior of energetic devices. For this reason, the results presented here are not envisioned as a substitute for large-scale verification testing. Rather, a final goal of this effort was:

4. Determine if and how reduced-scale explosive device testing can be applied to accelerate development of experimental diagnostics and predictive models.

In the following sections, progress toward each of these goals is briefly discussed with reference to details available in several publications that have resulted from these efforts [17-25].

This page left blank

2. EXPERIMENTS

2.1. Explosive Detonators

The existing literature primarily considers devices made up of 100s of grams to many kilograms of explosive material surrounded by a comparable mass of metal casing. While such experimental scales are of immediate relevance to many applications, they also produce hazardous testing environments with costs that may preclude experimental repetition. Instead, here gram-scale experiments are proposed based on commercially available exploding bridgewire (EBW) detonators. Most results presented here utilize the RP-80 EBW detonator from Teledyne RISI [26], shown schematically in Figure 1. In this device, an EBW first ignites 80 mg of pentaerythritol tetranitrate (PETN). This subsequently initiates a 123 mg output pellet of nitramine hexahydro-1,3,5-trinitro-1,3,5-triazine (Royal Demolition Explosive, RDX). In the standard configuration, an inner cylindrical brass sleeve surrounds both pellets, and a 0.18 mm thick aluminum cup encases both the brass sleeve and the flat end of the output pellet. Some of the experimental results presented here utilize slightly modified versions of the RP-80 also purchased from Teledyne RISI, including versions without the aluminum cup and some with a clear plastic sleeve in place of the brass sleeve.

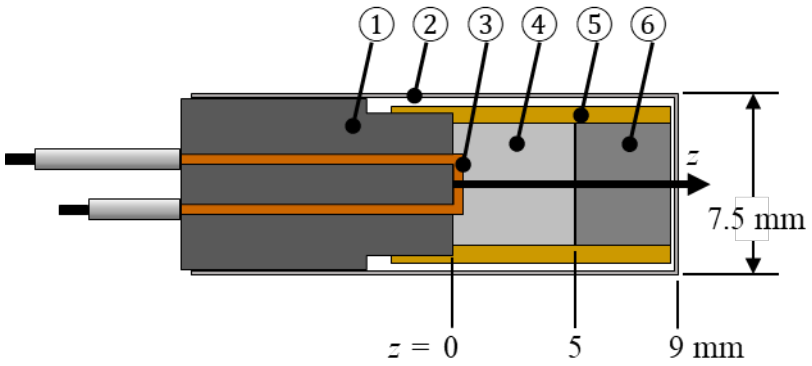

Figure 1: Simplified schematic of the RP-80 EWB detonator, where main components include (1) plastic molded header, (2) aluminum cup, 0.18 mm thick, (3) bridgewire (gold), (4) initiating explosive: 80 mg PETN, (5) brass sleeve, (6) output explosive: 123 mg RDX. Drawing is not to scale.

Prior literature considering the RP-80 detonator can be classified into two general thrusts. The first and most extensive research thrust focuses on the design and characterization of detonators for their intended purpose of explosive initiation. A recent review is provided by Rae and Dickson [27], with the extensive reference list therein giving many details. Recent notable experimental work includes the efforts by Smilowitz *et al.* [28, 29] who performed visible and x-ray imaging of reaction wave propagation within RP-80 detonators. The second and much less extensive research thrust utilizes RP-80s and similar detonators as sub-scale test platforms for diagnostic and model development. Recent examples include Monat *et al.* 2014 [30] who used the RP-80 as a test platform to demonstrate a novel pressure gauge; Granholm and Sandusky [31] who utilized a RP-80 to evaluate shock reactivity in small energetic samples; and Fouchier *et al.* [32] who used an RP-80 as a sub-scale experiment for blast loading in urban environments. The work reported here extends upon the concept of this second thrust by demonstrating application of the RP-80 to post-detonation fragmentation and fireballs.

2.2. Overall Phenomenology

The remainder of section 2 summarizes experimental results and diagnostic developments obtained during the 2018-2020 Sandia LDRD project. The current sub-section provides some qualitative imaging of the overall phenomenology, while remaining sub-sections provide more quantitative measures of case fragmentation and the post-detonation fireball.

Figure 2 images the luminosity from the propagating reaction waves within an RP-80 with a clear plastic sleeve and no cup. Experiments presented in Figure 2 replicate the prior work of Smilowitz [28, 29]. The first image was recorded prior to the detonation and shows the initial geometry. The remaining eleven images where recorded at 10 MHz with a Shimadzu HPV-X2 camera. Raw images are grayscale and are false colored in Figure 2 to enhance visibility.

In all experiments presented here, detonators are initiated with a FS-43 fireset from Teledyne RISI [33]. This fireset sends a high-voltage pulse to the bridgewire, which bursts and ignites the PETN input pellet at about t = -1.4 μs in Figure 2. The ensuing reaction wave travels from bottom to top in the orientation shown in Figure 2. At approximately t = -0.4 μs, the reaction wave transitions into the higher density RDX output pellet. Finally, at t = 0 μs, the reaction wave reaches the end of the output pellet and launches post-detonation products into the surroundings.

For experiments reported here, bridgewire voltage/current histories were not recorded. Consequently, the instant of bridgewire burst is not well resolved, and, in contrast to much of the prior work, the instant of bridgewire burst is not used as t = 0. Instead, in Figure 2 and all experimental results presented here, the first distinguishable release of products from the top of the detonator (or first motion of the aluminum flyer in experiments with an aluminum cup), is defined as t = 0. Compared to alternative choices for t = 0, such as the fireset trigger time, the first instant of product release is found to produce the least shot-to-shot jitter.

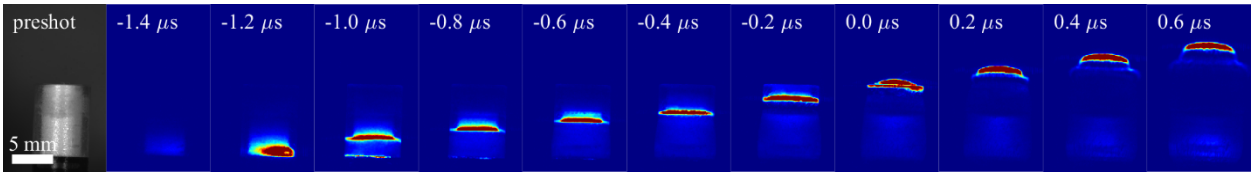

Figure 2: Emission from a RP-80 EBW with a clear plastic sleeve showing internal ignition and propagation of the detonation wave, false colored.

Figure 3 shows backlit imaging of a RP-80 detonator with aluminum cup at times following the internal dynamics shown in Figure 2. Figure 3 images were recorded at 1 MHz with a Shimadzu HPV-X2 camera, backlit with a Cavilux Smart UHS laser (640 nm central wavelength, 50 ns pulses synchronized with the camera frames). To reject most emission from the post-detonation fireball, the camera lens included a 640±10 nm bandpass filter. For reference, the z origin in Figure 3 designates the location of the bridgewire at the interface between the plastic molded header and the input pellet.

As shown in Figure 3, in the first few μs after detonation the metallic case rapidly expands and eventually breaks into many fragments. The largest (mm-scale) fragments originate from breakup of the cylindrical brass sleeve and propagate outward in an approximately axisymmetric ring. Quantitative measures of this case deformation and fragmentation are presented in sub-sections 2.3 and 2.4, respectively.

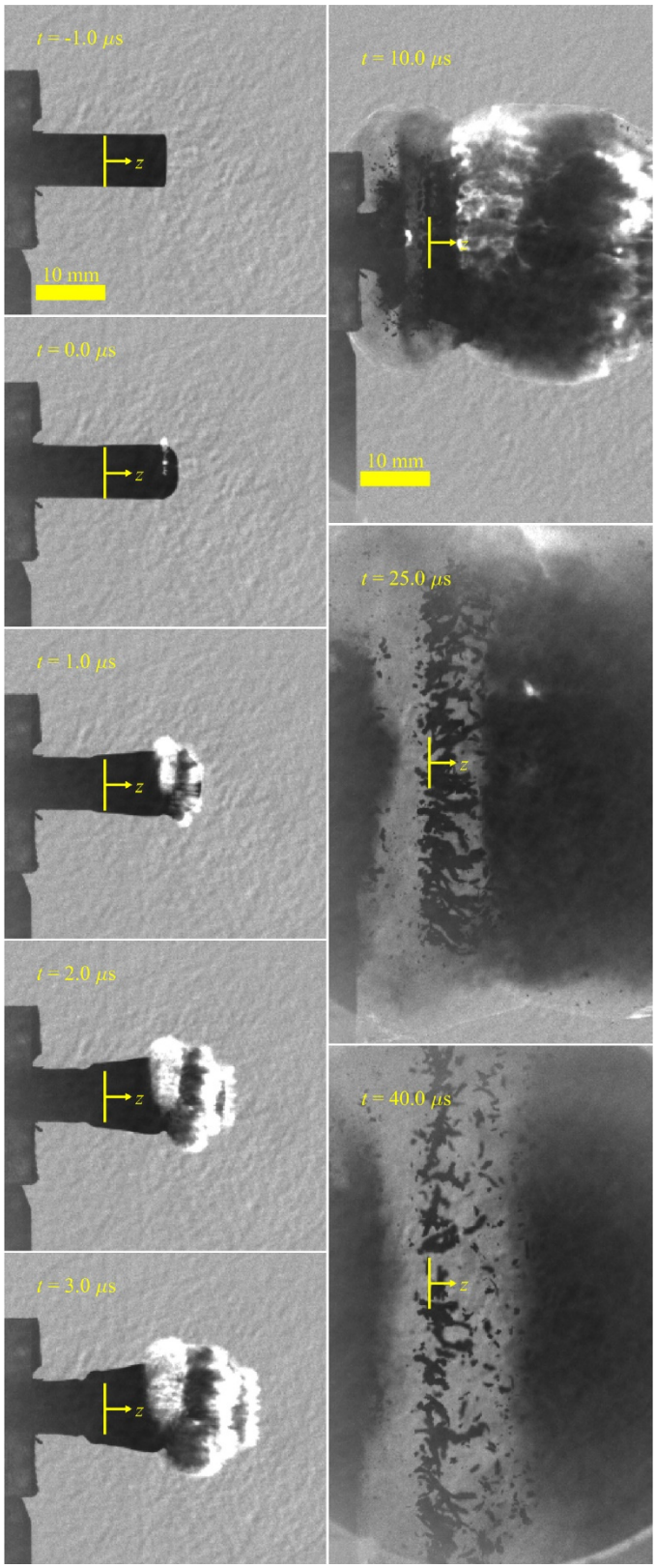

Figure 3: Typical backlit imaging of the detonation of a RP-80 EBW with aluminum cup showing case fragmentation and generation of an afterburn fireball.

Concurrently, the hot products of detonation are released from the flat end of the output pellet. As shown in Figure 3, this results in a luminous post-detonation fireball that persists for a few 10s of μs. To quantify the behavior of this fireball, sub-section 2.5 presents detailed imaging along with quantitative measures of spectral emission. Following this, sub-sections 2.6 and 2.7 demonstrate laser diagnostics for quantitative measures of fireball temperatures and particulates, respectively. Finally, section 2 concludes with the demonstration of detonators containing unique chemistries that significantly modify the fireball behavior.

2.3. Case Deformation

For the quantification of case and fragment motion in explosive device testing, widely applied experimental techniques include photonic Doppler velocimetry (PDV) [3, 8, 34, 35], high-speed videography [3, 4, 8, 34-36], and pulsed x-ray imaging [3, 37, 38]. PDV provides exquisite time resolution of case velocity with good precision but is a point measurement that offers limited spatial resolution. Conversely, visible and x-ray imaging can deliver spatial resolution but record much more slowly than PDV. Additionally, most literature examples rely on manual image processing [3, 4, 8, 34, 35, 37, 38]. Consequently, visible and x-ray image measures may be subject to uncertainties that are difficult to quantify. Finally, witness plates have also been used to estimate fragment velocities [39]. While relatively low cost and simple, witness plates only provide a mean fragment velocity based on time-of-arrival.

Digital Image Correlation (DIC) quantifies 3D surface motion by tracking unique surface patterns [40]. In the study of solid mechanics, DIC is relatively well-known and widely applied. Several commercial vendors are available for the required experimental hardware and processing algorithms. Recently, DIC measures of explosive devices and other very high-speed events have benefited from the emergence of ultra-high-speed cameras for imaging at 100s of kHz up to MHz frame rates. A few literature examples are given in [41-44].

In the current work, DIC techniques were extended to quantify the case deformation during the first few μs following detonation of an RP-80. Figure 4 shows typical experimental images. Prior to an experiment, the surface of an RP-80 with aluminum cup was painted white and then hand-dotted with a black marker. Case motion following detonation was recorded at 5 MHz using two Shimadzu HPV-X2 cameras orientated in a narrow stereo angle. Detonators were illuminated with three Cavilux Smart UHS lasers (640 nm central wavelength, 120 ns pulses synchronized with the camera frames). Each camera lens had corresponding 640±10 nm bandpass filters. Furthermore, to reduce specular reflections, the illumination lasers were orthogonally polarized with respect to camera lenses with the use of polarizing filters.

Figure 5 summarizes the 3D surface deformation quantified from the example images shown in Figure 4. Many more details on the experimental and data processing techniques are available in several publications resulting from this work [17, 23]. Overall, Figure 5 results and details in [17, 23] demonstrate that DIC with the latest ultra-high-speed cameras can resolve deformation of the explosively loaded case with good precision and accuracy. In addition, the properly shielded DIC configuration does not require any significant experimental modification between shots. In comparison, direct contact probes, such as PDV, are typically destroyed by the explosive, requiring extensive rebuild between experiments. Consequently, once constructed, the DIC configuration also allows for rapid experimental repetition. Therefore, the current results (and the more detailed findings in [17, 23]) demonstrate that DIC is well suited for precise case deformation measurements while enabling experimental repetition.

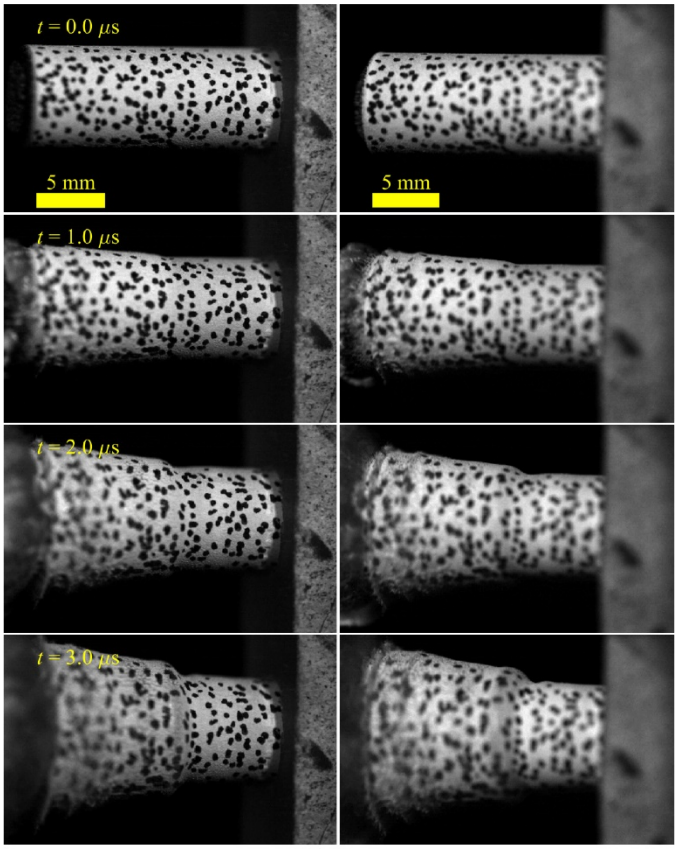

Figure 4: Typical Digital Image Correlation (DIC) video frames of a RP-80 with aluminum cup from the (left) and (right) stereo cameras, respectively.

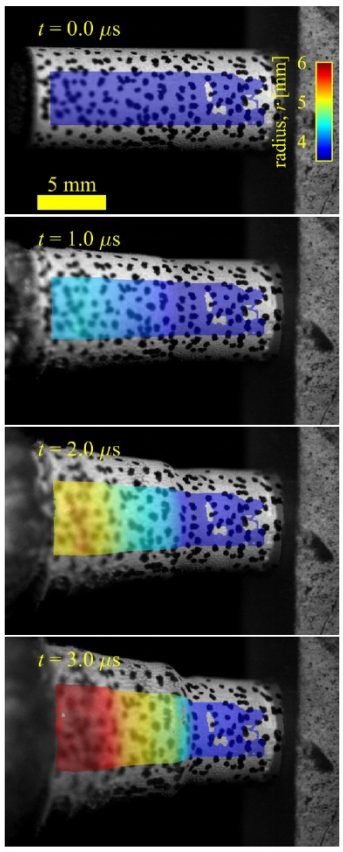

Figure 5: Digital Image Correlation (DIC) overlaid with measured case radius (color scale).

2.4. Case Fragmentation

In the literature, fragment masses and dimensions are often measured by collection [3, 4, 8, 34, 36, 39, 45-49]. To decelerate and capture high-velocity fragments, these techniques use a variety of soft-catch materials (sawdust, cardboard, Styrofoam, etc.) positioned around the explosive device. After a test, fragments are manually located within the catch material and then individually weighed and sized. Fragment collection may be subject to biases due to secondary breakup upon impact with the catch material. In addition, this method is time consuming, making experimental repetition difficult.

In this work, an experimental configuration that utilizes only high-speed imaging is presented for quantification of fragment sizes and velocities. While image-based tracking and sizing of particles is a relatively mature technology for several research fields, prior application to explosively generated fragments has been limited. Critically, few (if any) prior studies have attempted an in-depth assessment of measurement uncertainty. Due to the unique challenges arising from highly non-spherical fragment morphologies, shock waves, and experimental hazards, dominant measurement uncertainties for the image tracking of explosive fragments may significantly differ from uncertainties reported in the literature for particle tracking in other applications.

Here (and in more in-depth publications resulting from this work [17, 23]), 3D tracking and sizing of fragments is performed with a stereo Shimadzu HPV-X2 camera configuration similar to the DIC configuration but viewed at a radial location away from the RP-80 detonator where individual fragments pass through the fields of view. Figure 6 shows select results, which were recorded at 2 MHz and backlit with the aforementioned Cavilux Smart lasers.

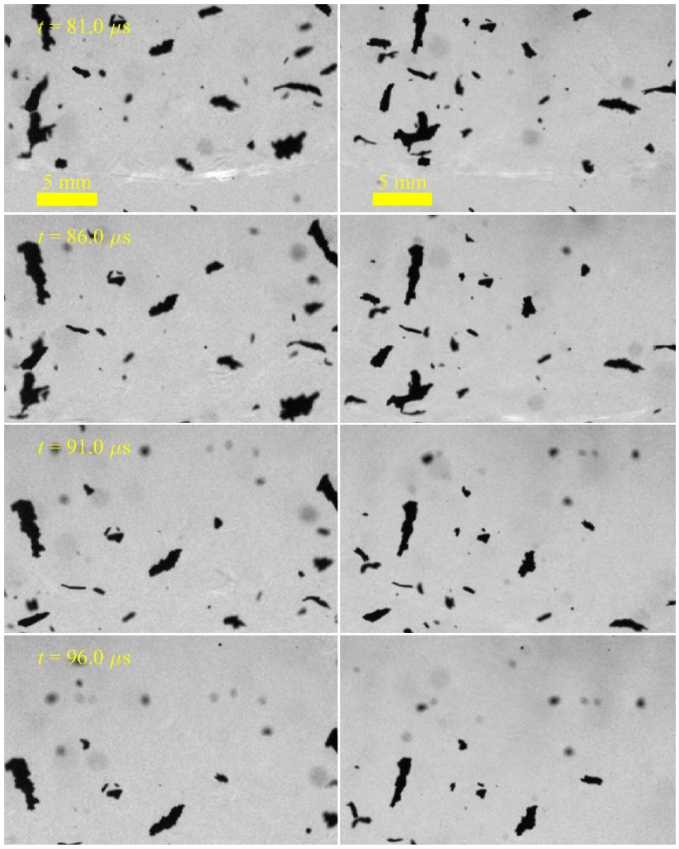

Figure 6: Typical backlit fragment tracking video frames from the (left) and (right) stereo cameras, respectively. Detonator is a RP-80 EBW with aluminum cup, initially placed end-on approximately 76 mm above the views shown here.

As discussed further in [17, 23], image processing first locates the fragment silhouettes in each frame. Next, 2D fragment trajectories are identified for each video using the methods in [50]. Finally, stereo triangulation is used to combine the 2D trajectories from the left and right fields of view into 3D trajectories. Figure 7 shows example results for the images shown in Figure 6.

As illustrated in Figure 7 fragments from naturally fragmenting explosive devices (without scores or features to promote fragmentation along predetermined paths) tend to be highly non-spherical, often with one thin dimension that corresponds to the case thickness at failure [51, 52]. This greatly complicates attempts to measure fragment volumes (therefore masses) from 2D silhouettes. Developments to address these issues are discussed further in [17]. There, a 3D surface triangulation is proposed to account for the unique morphologies of explosively generated fragments. In [17] simulations and experimental results are presented that demonstrate quantitative improvements in the accuracy of measured fragment volumes.

As an alternative to visible imaging, the work reported here has also explored the use of x-ray imaging for fragment measurements. Figure 8 shows select results. Here an RP-1 detonator, also from Teledyne RISI [53], is studied. Six flash x-ray heads were used to record the fragment field at six unique times after detonation. These x-ray heads were bundled into two distinct perspectives (distinguished by the top and bottom rows in Figure 8). By assuming linear trajectories, [21] proposed new processing methodologies that quantify the 3D fragment trajectories from data such as shown in Figure 8. In addition, because x-ray absorption is proportional to the line-of-sight mass, the preliminary

developments reported here may also be extendible for accurate fragment mass measurements [22], overcoming some of the challenges of visible imaging discussed above.

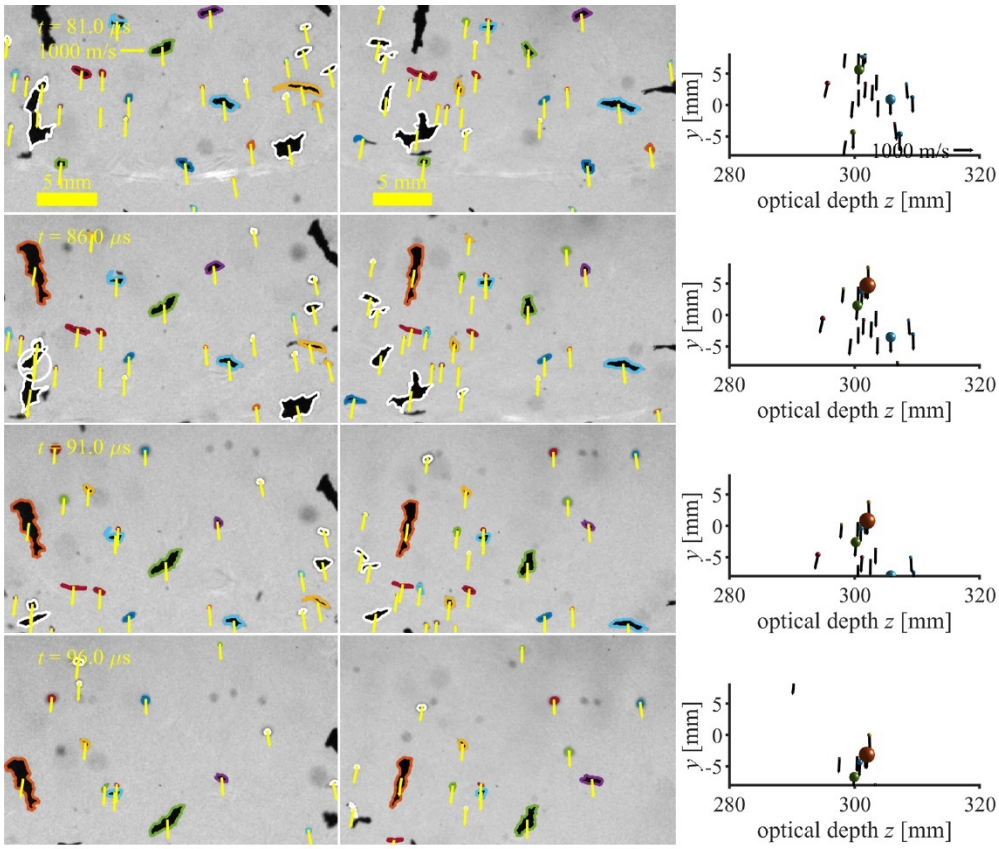

Figure 7: Fragment tracking overlaid with outlines showing detected fragments and colors indicating correspondence between left- and right-FOVs. Yellow arrows show two-dimensional velocity vectors. The right-most column is a triangulated out-of-plane view.

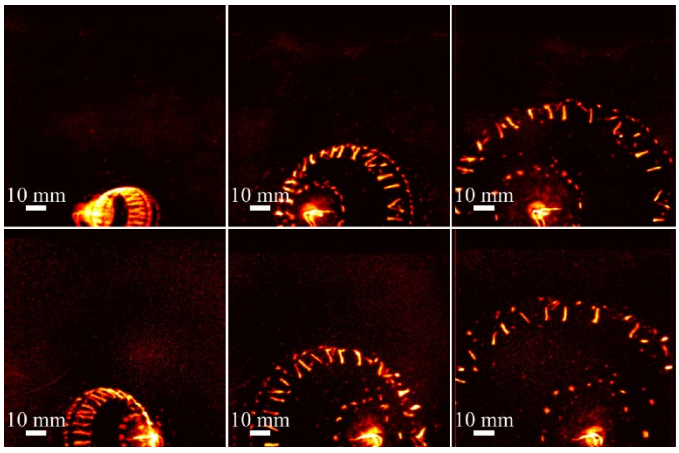

Figure 8: Flash X-ray images (false colored) of fragment from an RP-1 detonator from Teledyne RISI [53]. Images were recorded at six unique times and two unique perspectives (differentiated by the top and bottom row).

The discussion in the current and previous sub-sections provides a brief overview of advancements in imaging diagnostics for the deformation and fragmentation of explosively loaded metal cases. As demonstrated above, and further clarified in publications resulting from this work [17, 23], gram-scale explosive test articles allow for rapid turnaround experiments, accelerating development and validation of advanced diagnostics, as was postulated in section 1.

2.5. Fireball Structure and Emission

In a typical explosive device only a fraction of the available chemical energy is consumed at the detonation front, and remaining energy is released by the products of detonation. These products may mix with the surrounding environment and oxidize, forming what is often referred to as a post-detonation fireball [1, 54]. Prior to this work, most published experimental investigations of post-detonation fireballs have considered test articles consisting of at least 10s of grams of explosive material [10, 55-58]. As discussed above, these larger-scale test articles have direct relevance to many applications. However, diagnostics also tend to be limited by the experimental scales, harsh environments, and outdoor test arenas.

Figure 3 already demonstrated that post-detonation fireballs generated by the RP-80 detonator display qualitative similarities to larger-scale tests. In this sub-section, additional imaging and emission diagnostics are presented. Figure 9 summarizes three ultra-high-speed imaging diagnostics, which have been applied to detonator scale experiments for the first time. All data were recorded at 1 MHz using a Shimadzu HPV-X2 camera. The top row of Figure 9 shows the fireball emission as recorded by the camera with a typical photographic lens. Images provide a qualitative visualization of the emission integrated across the full spectral sensitivity of the camera's silicon detector. The middle row in Figure 9 was recorded by a knife-edge schlieren configuration [59, 60] that provides line-of-sight visualization of the index-of-refraction gradients in the flow. These schlieren images clearly visualize the leading shock wave, including spatial and temporal variations. Finally, the bottom images of Figure 9 were backlit with diffuse and spatially uniform light. In this configuration, images primarily visualize absorptive features in the flow, likely solid particulates and soot in this case.

To further quantify the optical emission, Figure 10 shows results from the custom, high-speed "pyrometer" detailed in [20]. This experimental configuration uses a high numerical aperture, multi-mode fiber to collect spatially integrated emission. Fiber output is collimated and divided into multiple wavelengths using a series of optical beam splitters and bandpass filters. The temporal responses of individual wavelength bands are recorded by fast photodiodes and digitized by an oscilloscope. As demonstrated in Figure 10, measurements provide detailed quantification of the emission time history, revealing two distinct emission peaks. A first peak starting at $t = 0$ corresponds to the initial release of the detonation products. This first peak quickly decays as the primary shockwave and product cloud expand. The emergence of a second peak at around 10 to 15 μs may be indicative of oxidation within the post-detonation fireball, leading to heat release and increased luminosity at later times.

Finally, the spectral content of the fireball is further visualized by the results shown in Figure 11. Each row of Figure 11 shows select images from 2 MHz videos recorded with the Shimadzu HPV-X2 camera equipped with the indicated bandpass filters. Spectral sensitivity for each wavelength range has been calibrated against a blackbody source, and the color scale in Figure 11 is proportional to the absolute emission in the band.

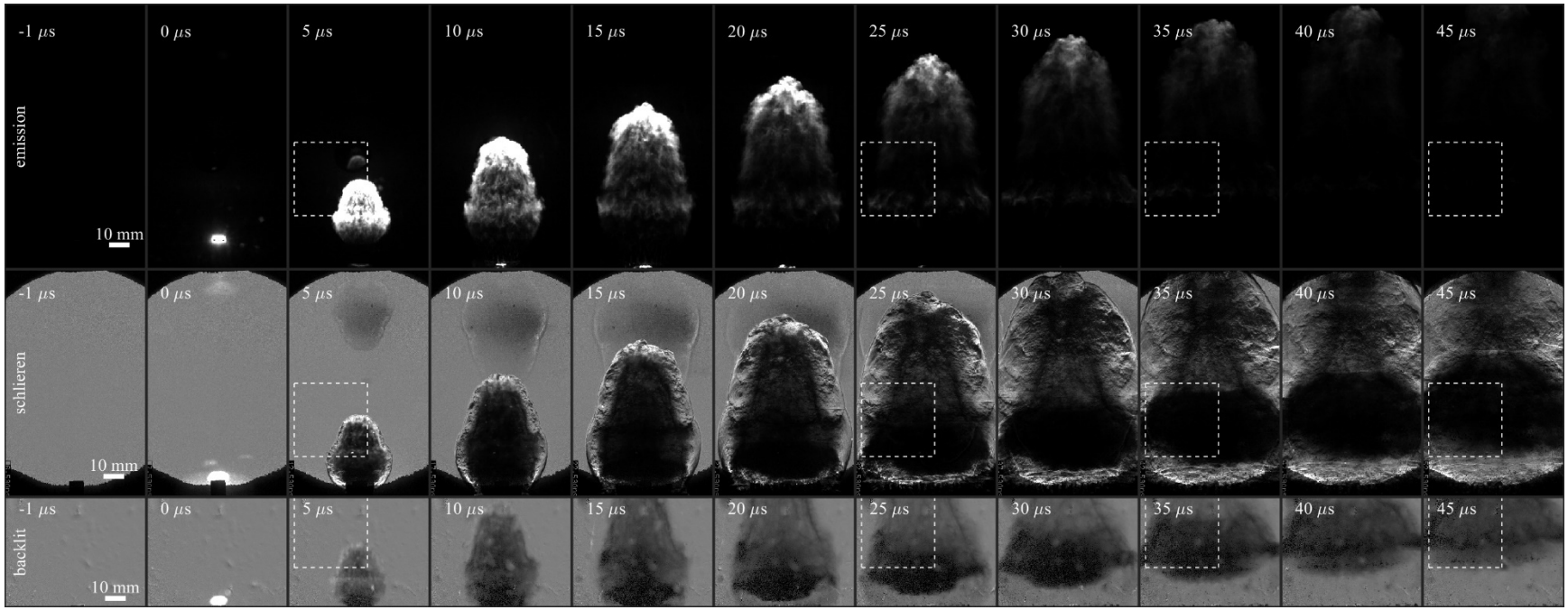

Figure 9: Experimental images highlighting the structure of the post-detonation fireball from an RP-80 EBW detonator without the aluminum cup. (top) visible emission captured by a Shimadzu HPV-X2 camera, (middle) schlieren illuminated at 640 nm with a horizontal knife edge and, (bottom) diffuse backlit imaging illuminated at 640 nm. Top and middle row were recorded simultaneously, while bottom row was recorded on a different experiment. Dotted boxes correspond to the approximate FOV of the LII images shown in Figure 16.

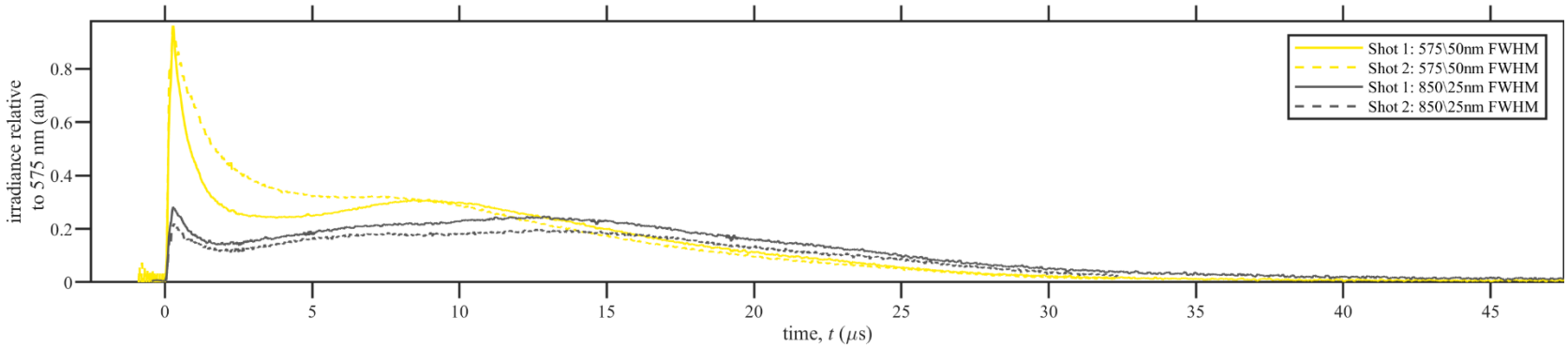

Figure 10: Integrated emission from the detonation of an RP-80 without the aluminum cup. Data shows two experimental repetitions [20].

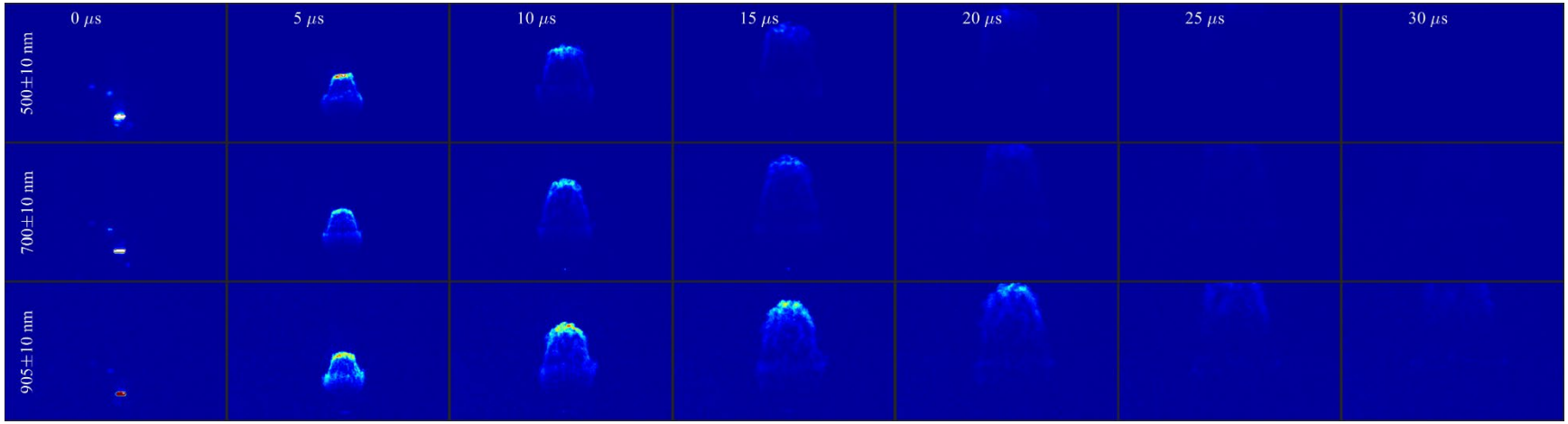

Figure 11: Wavelength filtered emission from the detonation of an RP-80 without an aluminum cup, false colored. Each row corresponds with a different experimental realization. Color scale is proportional to absolute emission. White indicate saturated pixels.

2.6. Fireball Temperatures and Species Concentrations

Gas-phase temperature measurements were performed in the post-detonation fireball from an RP-80 without the aluminum cup using an ultrafast laser spectroscopy technique. Results from these experiments have been reported in two journal publications [18, 19] and are only briefly summarized here. The detonator was contained in a polycarbonate enclosure with glass windows for laser access. A schematic drawing of the laser system and enclosure is shown in Figure 12. Fireball temperatures were measured 35–40 mm above the detonator, 12–25 mm radially outward from the detonator centerline, and at $t = 18$ and 28 μs. Light scattering from particulate and solid fragments was a significant challenge and was mitigated using a new polarization scheme to isolate the laser signal [18].

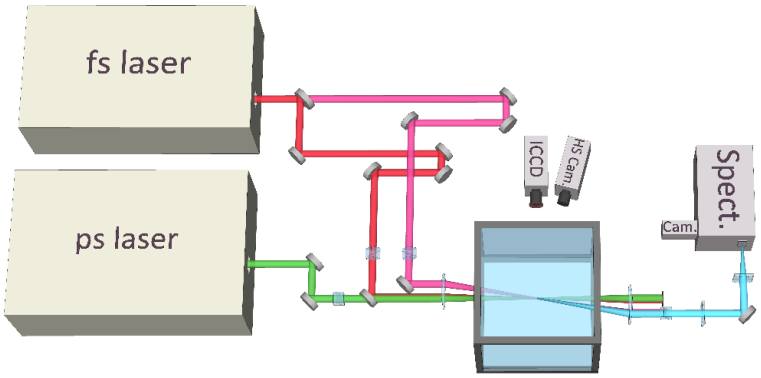

Figure 12: Schematic of the laser system used to perform gas-phase temperature measurements in the detonator fireball.

A hybrid femtosecond-picosecond (fs/ps) rotational Coherent Anti-Stokes Raman Scattering (CARS) instrument was used to acquire approximately 100 temperature measurements along a 5 mm tall line in a single laser shot. An example CARS spectrogram is shown in Figure 13 along with two examples of the spectral fitting to obtain quantitative temperature values. Initial measurements of the fireball temperatures were in the range 300–2000 K with higher temperatures occurring 28 μs after detonation as shown in Figure 14.

These laser-based temperature measurements are a new measurement capability developed for benchtop-scale explosives under this LDRD project. Future work will compare the experimental temperature data to simulations. Some of the uncertainties associated with this temperature data are as follows: (1) The measurement volume was about 2.8±0.7 mm long and the CARS spectra represent weighted temperatures over this measurement volume. (2) The spectra are preferentially weighted to colder gases. Also, the exact Raman excitation efficiency for the different Raman transitions is difficult to determine as the lasers traverse the fireball environment and are chirped or distorted. Finally, (3) due to the stochastic nature of turbulent detonator fireballs, many detonator tests would be required to fully characterize the fireball temperatures. Such extensive testing was outside the scope of this project. Additional testing at other spatial locations and times within the fireball are required to fully map out the temperature field and its evolution.

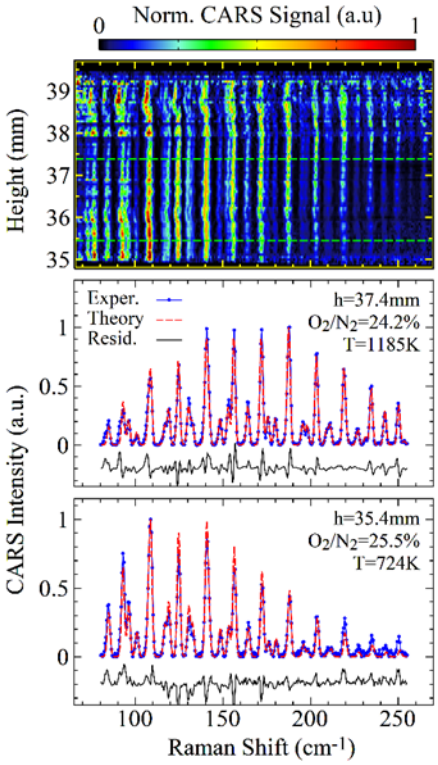

Figure 13: Example spectrogram and fitting results for CARS thermometry in the detonator fireball.

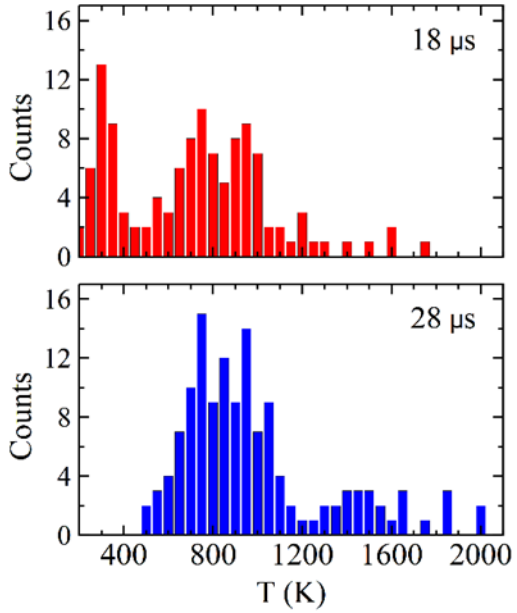

Figure 14: Histograms of CARS temperatures in the detonator fireball at two different times after initiation.

As an alternative to laser diagnostics, prior work by Lewis *et al.* [61, 62] has demonstrated fireball temperature measures using seeded atomic emission. A preliminary demonstration of similar capabilities for RP-80 detonators is shown in Figure 15. In this experiment, a thin copper flyer was initially affixed to the output end of an RP-80 without aluminum cup. A CP-140 spectrometer was

used to record the optical emission resulting in the raw experimental image shown at the top of Figure 15. As was done in Lewis *et al.* [61, 62] measured emission was fit to a model, estimating the apparent temperature of ~5600K as shown in the bottom of Figure 15. Note, this experiment was intended only as a demonstration of capability. The exact effect of the copper flyer on the fireball dynamics is unknown. As done in Lewis *et al.* [61, 62], future and more in-depth experiments could extend this work by directly mixing atomic tracer materials into the explosive formulations.

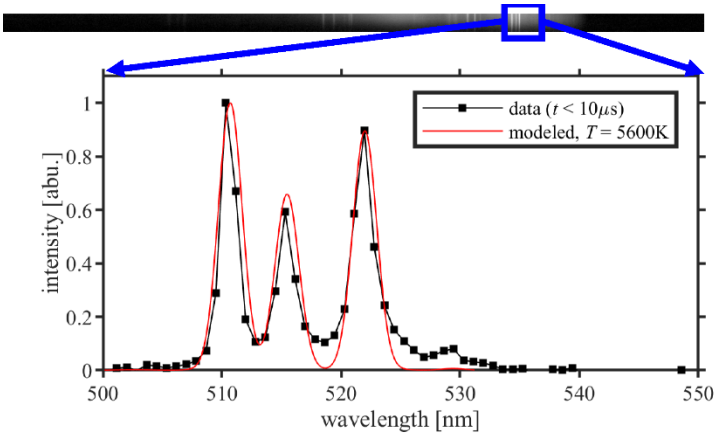

Figure 15: Emission spectrum from the detonation of an RP-80 with a copper flyer initially affixed to the output face. (top) Example experimental image and (bottom) quantitative results over a select wavelength range including the best-fit modeled spectrum.

2.7. Fireball Soot and Particulates

As demonstrated by the bottom row in Figure 9 the RP-80 fireball includes a cloud of solid particulates. Similar particulate clouds have been observed in much larger-scale experiments [10, 63-68] and have been postulated to consist of carbon soot as well as remnant, potentially partially reacted, explosive material [63-65]. In addition, particulates are assumed to be a dominant source of optical emissions in the visible and near infrared [10, 68]. Therefore, quantification of particulate behavior is critical to the derivation and validation of emission models [66, 67]. Unfortunately, due to the many practical challenges of large-scale testing, experimental measures of fireball particulates are limited [63-65].

Laser Induced Incandescence (LII) is an experimental diagnostic for soot that is widely applied in fundamental combustion studies [69, 70]. The current work reports on what is believed to be the first attempt at LII measurements in a post-detonation fireball from a detonator. In the LII variant considered here, the 1064 nm output from an 8 ns duration Nd:YAG laser (Spectra Physics, Quanta Ray Pro 350) was formed into a thin sheet. Synchronization electronics were used to pulse the laser after a predetermined delay following the detonation of a RP-80 without the aluminum cup. Laser heating rapidly increases the temperature of particulates within the laser sheet, causing these regions to emit significantly above the background. This LII signal is imaged by an intensified camera (Princeton Instruments PI-Max), gated to integrate the emission for a 10 ns period during and immediately after laser heating. At the same time, a second intensified camera (Princeton Instruments PI-Max) was co-aligned through a beamsplitter along the same optical axis as the LII camera. This second camera was gated for 10 ns immediately before laser heating to image the background emission (aka self-emission).

Figure 16 shows select LII results. Each row presents images recorded from a different experimental realization in which LII was recorded at the times indicated on the left. The FOV approximately

corresponds with the dotted boxes shown in Figure 9 and the laser sheet passed through the axis of symmetry of the detonator. The top row of Figure 16 shows experimental results recorded shortly after detonation (t = 5 μs). At this instant, the LII image reveals significant radiation immediately behind the blast wave. Note, as shown by the background image recorded immediately prior to laser heating, some of the signal recorded near the tip of the blast wave is also due to self-emission. At later times in Figure 16, LII images show a distinct region of laser heated particulates and significantly lower background emission. Overall, Figure 16 results reveal that particulates in the flow are primarily confined within a narrow band behind the expanding blast wave. This banded structure is much less obvious in the more traditional imaging presented in Figure 9, highlighting an advantage of LII for improved mapping of particulate structures in the post-detonation fireball.

As discussed in a wealth of literature publications [69, 70], with proper calibration, LII can also provide quantitative measures of particulate concentration, size distributions, and other quantities of interest. These calibrations require some *a priori* information on the optical properties of particulate in the flow. For mature soot from hydrocarbon combustion, the required optical properties are relatively well established [71, 72]. However, much less is known about explosively generated soot. Without reasonable knowledge of the required optical properties, additional quantitative measures from the results in Figure 16 are not yet possible and are left for future work.

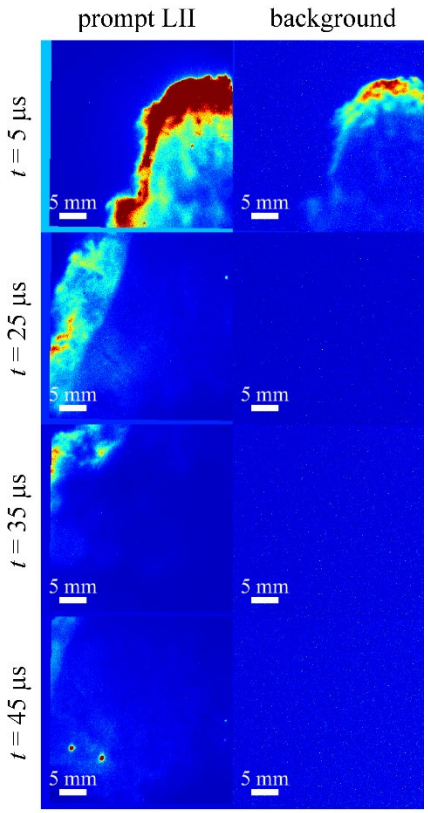

Figure 16: Laser Induced Incandescence (LII) from the particulates within the post-detonation fireball of a RP-80 without an aluminum cup, false colored. Field of view corresponds to the dotted boxes in Figure 9. (left column) prompt LII signal integrating the emission from 10 ns immediately after laser heating; (right column) background signal integrating the emission from 10 ns immediately before laser heating.

To improve understanding of the particulate matter emitted from RP-80 detonations, a preliminary experimental investigation was undertaken using kinetic/thermophoretic particle sampling with subsequent scanning electron microscopy (SEM) and energy dispersive X-ray spectroscopy (EDS) analysis. In a first set of experiments, copper SEM grids were positioned directly above an RP-80 without the aluminum cup. The relatively fragile copper grids were mounted inside a recessed metal housing to provide some degree of rigid backing and blast protection. Figure 17 shows typical post-test SEM/EDS results. The SEM image in the upper left panel of the Figure 17 (scale bar is 60 microns), reveal large particles with jagged edges, whose size is several 10s of microns. EDS elemental analysis of carbon, atomic oxygen, and silicon bands reveals that not all large-scale particles are carbon-rich "soot," as has been previously assumed for fireball models [10]. One carbon-rich particle, highlighted by the red circled region in the upper right panel of Figure 17, was selected for high-magnification SEM, with the results shown in Figure 18. The fine-scale carbon structure reveals round particles, with diameters ranging from 10s of nanometers to several microns in size. There appears to be very little agglomeration of these carbon particles—in stark contrast to the structure of flame-generated soot, which is typically composed of a two-dimensional fractal aggregate structure, with near-monodisperse primary particles of a few tens of nanometers, and fractal chains of hundreds of nanometers to a few microns [71].

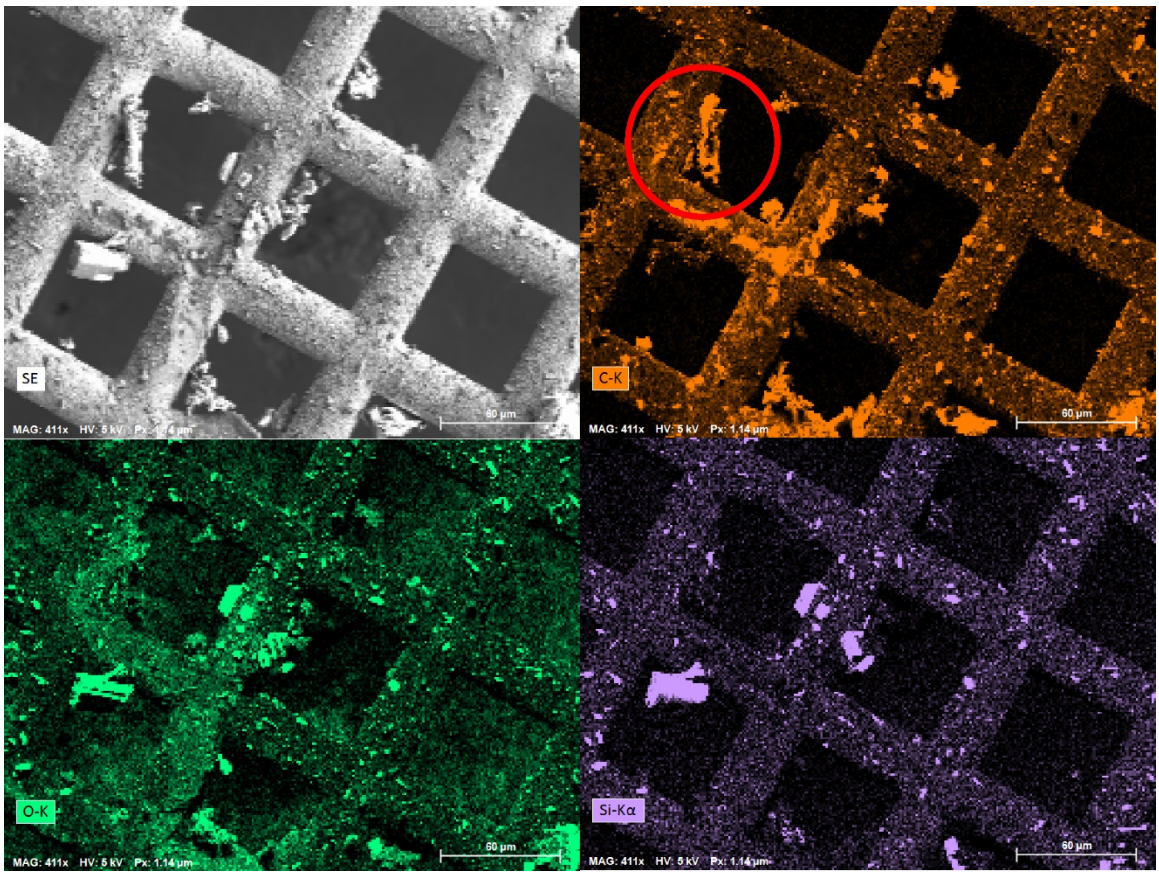

Figure 17: SEM (top-left) and chemically specific EDS imaging of particulate collected on a copper grid exposed to the fireball from the RP-80 without the aluminum cup. Red circle shows the area of high carbon content investigated at higher magnification in Figure 18.

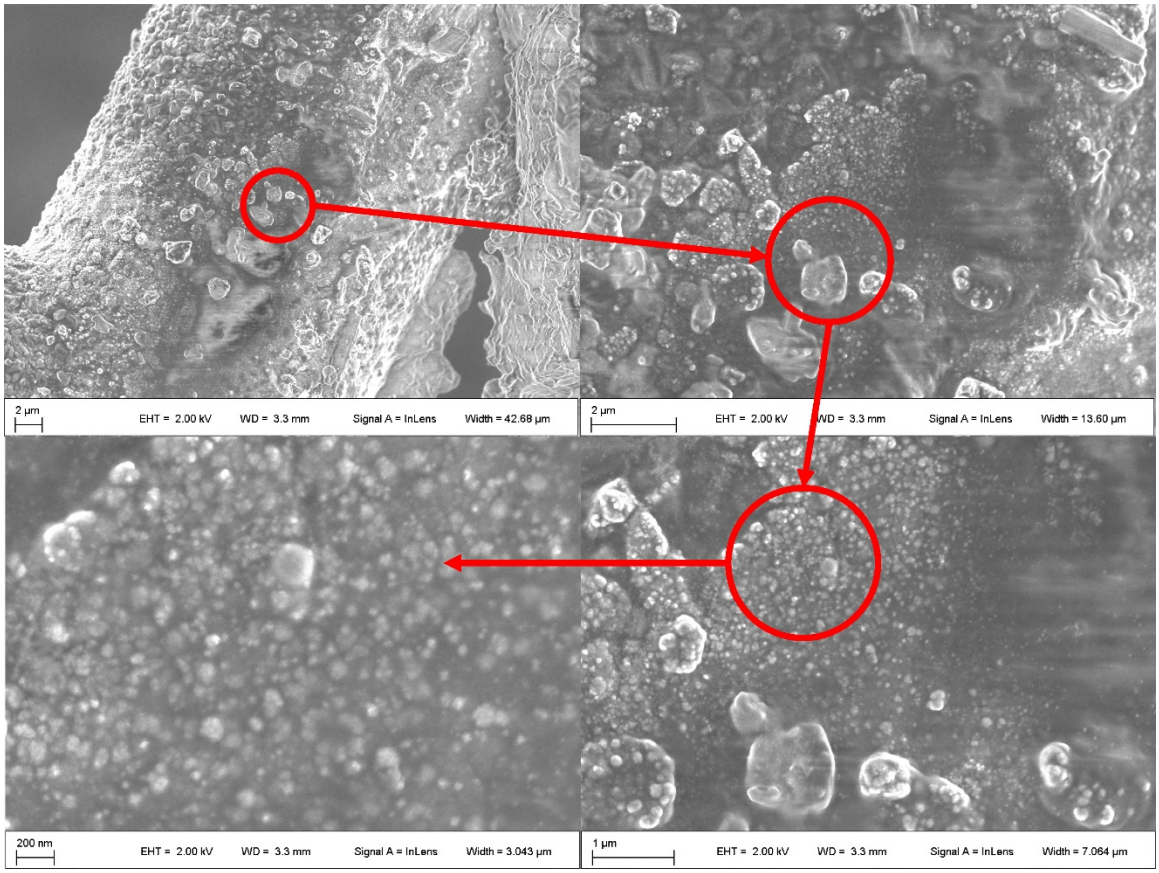

Figure 18: SEM imaging of the carbon rich region noted in Figure 17. Each image shows a higher magnification image of the area circled in red.

Additional particle sampling from RP-80 fireballs was conducted by exposing SEM stubs coated with carbon tape directly to the explosive products. This second round of particle sampling was conducted to improve particle collection, which could be inhibited by the protective SEM-grid holder used to collect the samples shown in Figure 17 and Figure 18. SEM stub sampling resulted in much more efficient particle collection, revealing several particulate types across a wide range of length scales. The particulates shown in Figure 19 are representative of the large-scale, jagged, often carbon-depleted matter observed previously on SEM grids in Figure 17. In other locations across the face of the SEM stub, much different particle morphologies with smaller length scales are observed. These small-scale features are shown in Figure 20, where carbon-rich structures appear to consist of fractal aggregates with submicron primary particles—familiar to flame-generated soot [71].

These particle-sampling studies support literature observations [63-65] that not all explosively generated particulates can be understood as carbon-rich "soot." However, questions remain. What is the time evolution of the particulate cloud? What are the refractive indices of the different types of particulates? Which kinds of particulates contribute most to emission, absorption, and scattering? For example, it may be that the small, rapidly heated particulates of the kind shown in Figure 20 are the main contributors to the LII signal and fireball emission, while larger and colder particulates attenuate fireball emission by increased scattering and absorption. All of these features may additionally act in a time-dependent manner, further complicating the physics.

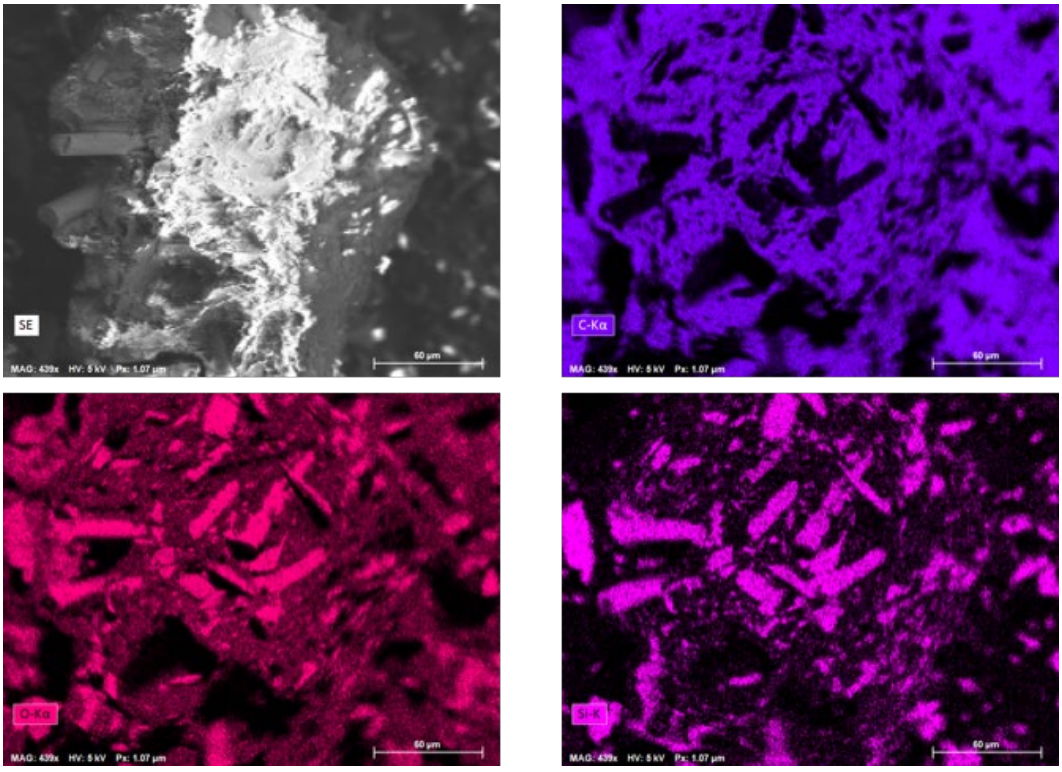

Figure 19: SEM (top left) and chemically specific EDS imaging of larger-scale particulate deposited onto an SEM stub coated with carbon tape and placed directly above an RP-80 detonator without the aluminum cup. The scale bar is 60 microns.

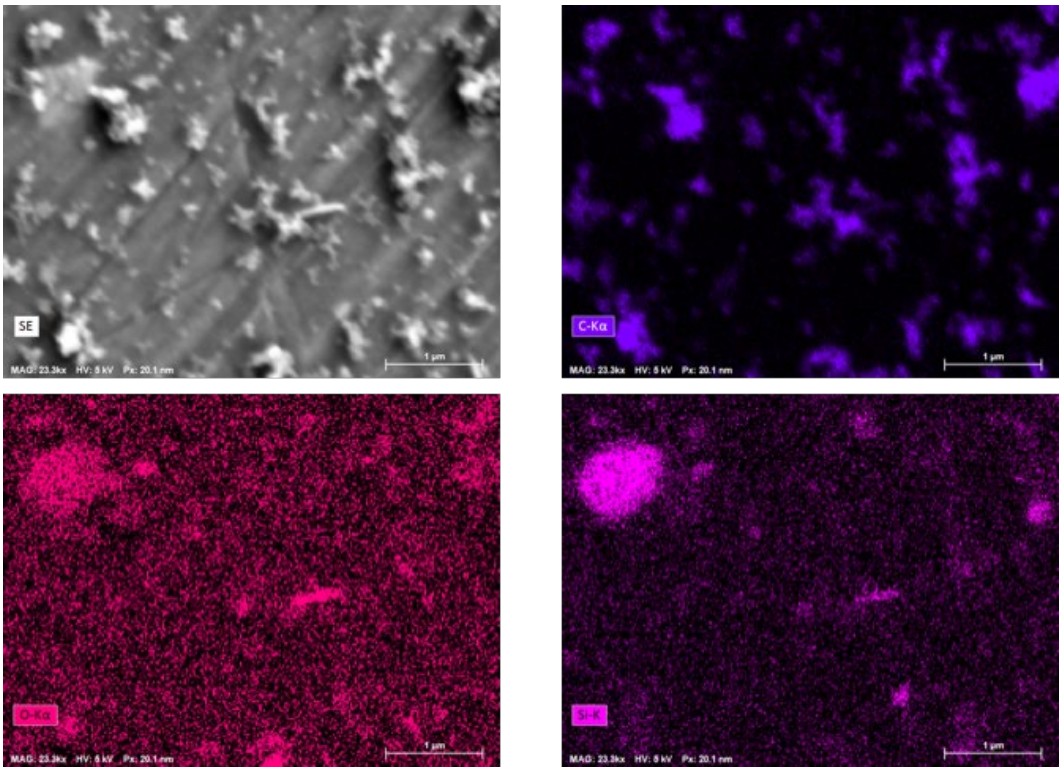

Figure 20: SEM (top left) and chemically specific EDS imaging of small-scale particulate deposited onto an SEM stub coated with carbon tape. The scale bar is 1 micron.

2.8. Custom Detonators

Finally, all experimental results presented thus far utilized commercially purchased detonators from Teledyne RISI. The LDRD project summarized by this report also explored the construction of customized explosive devices. To build these devices, only the RP-80 plastic molded header and bridgewire (items labeled 1 and 3 in Figure 1) were purchased from Teledyne RISI. At Sandia National Laboratories, these were combined with custom sleeves and explosive pellets. For example, Figure 21 shows a device consisting of a 0.9 gram/cm^3 PETN input pellet, a 1.6 gram/cm^3 PETN output pellet, and a 1.16 mm thick stainless-steel sleeve. Comparing Figure 21 with a similar visualization of the commercial RP-80 in Figure 3 reveals that the thicker stainless steel sleeve in Figure 21 fragments much differently than the thinner brass sleeve of the RP-80. In a second example, the top two rows of Figure 22 show emission and schlieren imaging of a device with a transparent plastic sleeve and the PETN pellets specified above. The bottom two rows of Figure 22 show a further modification where the output consists of a 1.6 gram/cm^3 pressing of PETN and aluminum in a 70/30 mass ratio. Comparing Figure 22 with a similar visualization of the commercial RP-80 in Figure 9 reveals that the custom explosive chemistries and plastic sleeves significantly alter the post-detonation fireball. As expected, the aluminized explosive in the bottom two rows of Figure 22 has a particularly dramatic effect on fireball luminosity and duration.

Figure 21 and Figure 22 results demonstrate that relatively simple modifications to the detonator configuration can significantly alter the post-detonation environment. In future work, customized devices, such as these, could be used to alter and study specific physical phenomena of interest. This could be particularly advantageous for the development and validation of models, which is the subject of the next section.

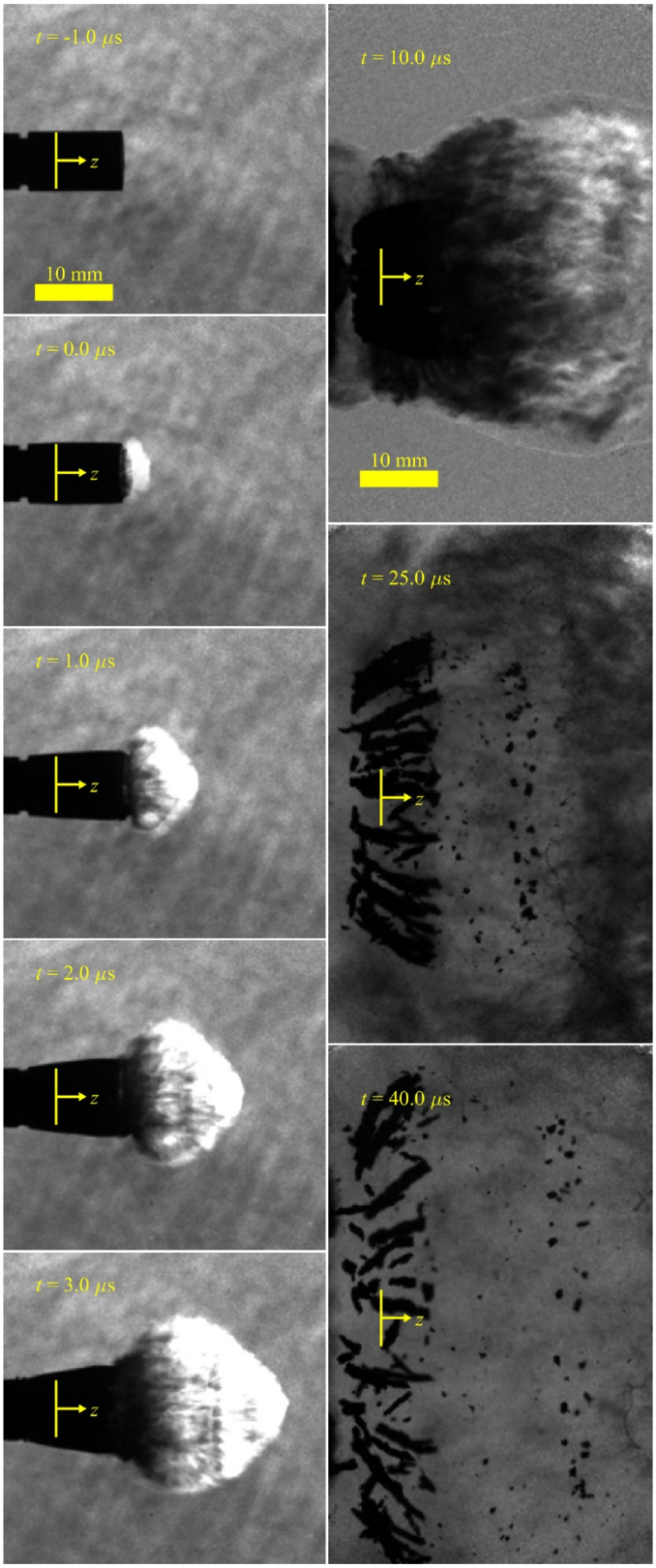

Figure 21: Typical backlit imaging of the detonation of a custom detonator with all steel case showing initial case deformation (left) and fragmentation into an outward propagating ring (right).

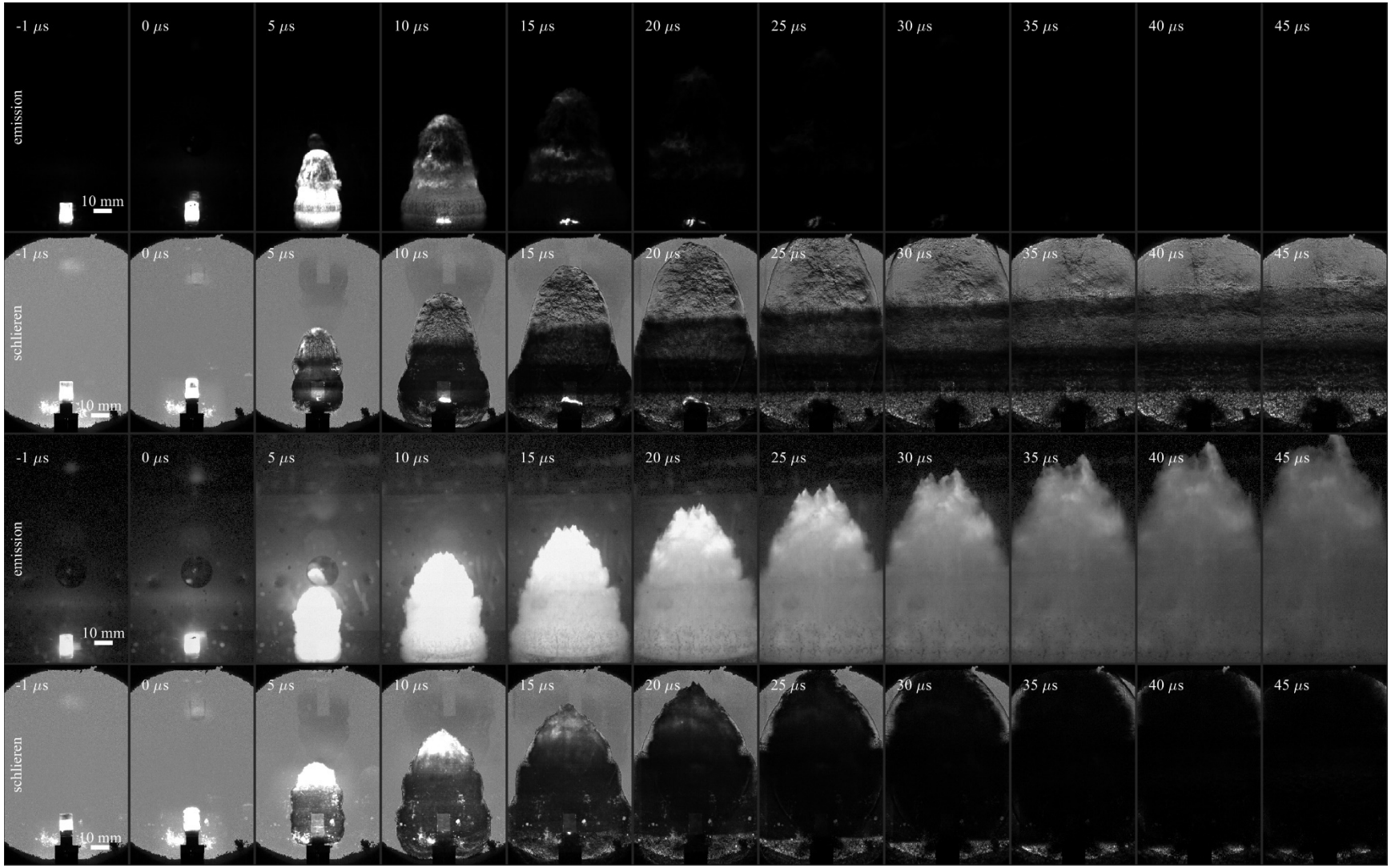

Figure 22: Optical emission and schlieren imaging of custom detonators. (top two rows) Custom detonator containing two PETN pellets in an optically clear plastic case. (bottom two rows) Custom detonator with an aluminized output pellet.

This page left blank

3. SIMULATIONS

Research efforts summarized by this report primarily focused on development of the experimental methods discussed above. Still, as outlined in section 1, a final goal of this work was to demonstrate if and how reduced-scale explosive device testing can be applied to accelerate the development and validation of predictive models. Toward this end, the current section briefly discusses modeling and simulations efforts performed.

3.1. Case Deformation and Fragmentation

To study case deformation and fragmentation, the RP-80 with aluminum case was modeled with the CTH hydrocode developed by Sandia National Laboratories [73]. The input pellet was modeled as PETN with a Jones-Wilkens-Lee (JWL) programmed burn model, while the output pellet was approximated as PBX9407 using a History Variable Reactive Burn (HVRB) model. The brass sleeve and aluminum cup were both modeled using a Mie-Gruneisen Equation of State (EOS) along with a Johnson-Cook strength and fracture model. The simulation domain was 3D and utilized adaptive mesh refinement (AMR). Finally, reactions were initialized at a point at the bottom of the input pellet.

Figure 23 summarizes simulation results. Overall, the case deformation, fracture, and fragment trajectories predicted in Figure 23 shows qualitative agreement with the experimental behavior in Figure 3. In [17], more detailed and quantitative model validation is performed using the DIC and fragment tracking results summarized in Figure 4 through Figure 7.

Importantly, Figure 23 and the detailed results in [17] demonstrate that a modern hydrocode can model the case deformation and fragmentation of the reduced-scale experiments described here. As discussed above, the current experimental configuration allows for significantly more advanced diagnostics and significantly reduced per-shot costs compared to larger-scale configurations commonly considered in the literature. Therefore, the capabilities developed here are expected to create new opportunities for model advancement, while also providing critical lessons learned when these measurement and simulation techniques are deployed on larger-scale configurations in future work.

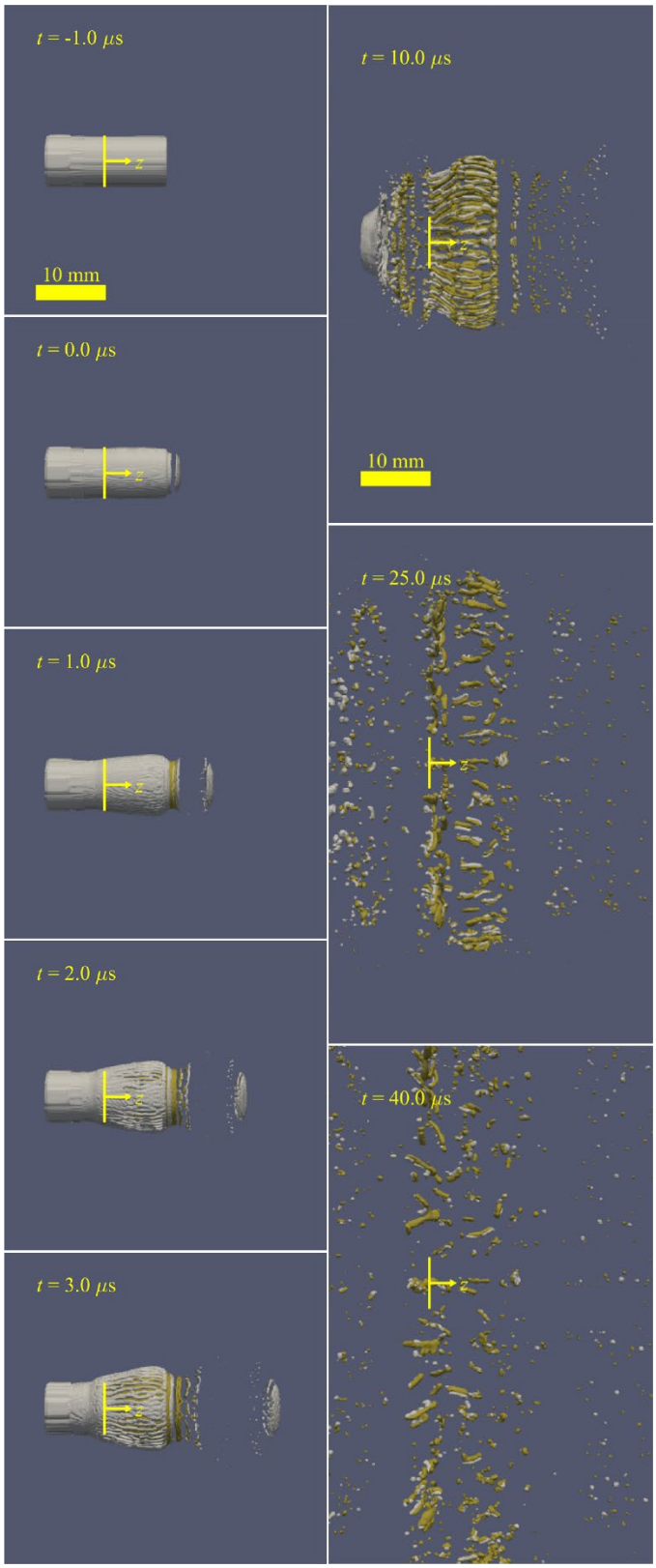

Figure 23: Simulation of a RP-80 EBW with aluminum cup showing initial case deformation (left) and fragmentation into an outward propagating ring (right) at times and fields of view corresponding to the experimental images in Figure 3.

3.2. Fireball Predictions

3.2.1. CTH Prediction of the Fireball

The CTH hydrocode methodology has also been applied to predict the structure of the post-detonation fireball as demonstrated in Figure 24. Consistent with the experiments presented in sections 2.5 through 2.7, simulations in Figure 24 considered a RP-80 without the aluminum cup. In this example, the surrounding is modeled as air that mixes with the detonation products approximated by the PETN and PBX9407 Equations of State (EOS) mentioned in the previous sub-section. Simulations do not include any post-detonation reactions and utilize artificial viscosity, which improves shock capture but does not accurately simulate turbulent mixing.

Despite the inherent limitations for modeling late-time fireball evolution, CTH predictions in Figure 24 show qualitative similarities to experimental observations in section 2. Specifically, the shock structure and propagation speeds predicted in Figure 24 are in reasonable agreement with the experimental schlieren images in Figure 9. In addition, CTH predictions show a high-pressure region surrounding a low-pressure central core. This appears consistent with the spatial distribution of particulates experimentally observed in Figure 16. Ongoing and future work will perform more quantitative comparisons between predictions such as Figure 24 and the experimental measures. Due to the known model limitations, comparisons are likely to identify phenomena that are poorly predicted by the hydrocode. This has already motivated some preliminary developments of alternative simulation techniques, as discussed in sub-section 3.2.3, below.

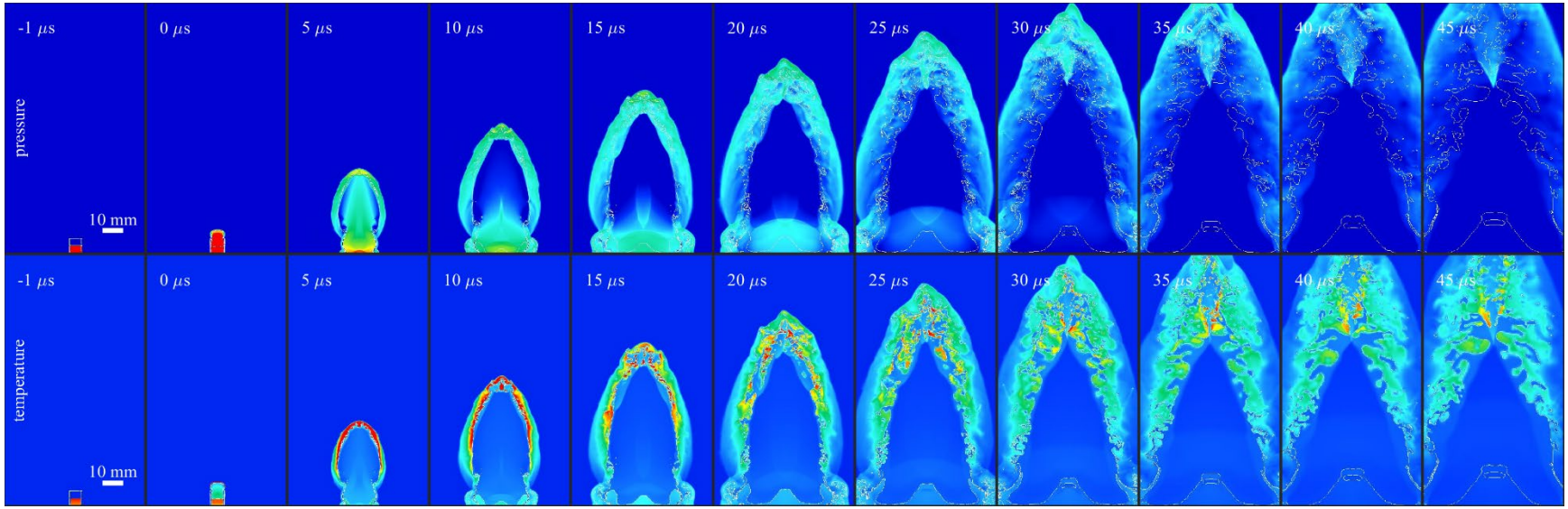

Figure 24: CTH simulations of a RP-80 EBW without an aluminum cup showing the predicted pressure (top) and temperature (bottom) contours for fields of view corresponding to the experimental images in Figure 9.

3.2.2. Emission Predictions

Optical emissions from detonators and larger scale explosive sources arise from complex and inter-related physical and chemical phenomena and are characteristic of device design and the environment in which it is detonated. Measurable emissions are spatially, temporally and spectrally dynamic, and individual diagnostic techniques can typically measure at most two out of three of these degrees of freedom (e.g., Figure 9-Figure 11). Here, optical emission predictions are generated by post-processing the CTH predictions in Figure 24 with Sandia's OPTSIG++ code. OPTSIG++ is a multi-material 3D ray tracing simulator that generates spatial, spectral, and temporal optical signals.

The OPTSIG++ configuration file sets up the viewing geometry relative to the explosive event (angle and distance of sensor, FOV, number of pixels, etc.) and generates a set of rays that spatially sample the fireball for every timestep. For each ray, OPTSIG++ solves the radiative transfer equation, which consists of the spectrally-resolved incident light, attenuation, and new emission for every ray segment (defined by the intersection of a ray with a hydrodynamic cell):

$$F_1 = F_0 e^{-\Delta\tau(T,\rho,\lambda)} + B(T,\lambda)\left(1 - e^{-\Delta\tau(T,\rho,\lambda)}\right). \quad (1)$$

In Eq (1) $B(T,\lambda)$ is the spectrally resolved Planck emission function and Δx is the path length [cm]. The spectrally resolved optical thickness of the segment is defined as $\Delta\tau(T,\rho,\lambda) = \kappa(T,\rho,\lambda)\cdot\rho\Delta x$, where $\kappa(T,\rho,\lambda)$ is the material spectral opacity [cm^2/g] and ρ is the density [g/cm^3]. OPTSIG++ can consider multiple materials in each cell based on the hydrodynamic or combustion simulation input.

Historically, materials are treated as continuum materials in the OPTSIG++ domain, but recently Sandia researchers added a graybody mist model to alternatively treat one or more materials as a 'mist'. In continuum models hydrodynamic variables (density, volume fraction, temperature, etc.) are used directly. For 'mist' materials the continuum variables are re-sampled into an ensemble of spheres based on two new optical post-processing variables: mist particle density and mist particle size. By selecting mist particle size and mist particle density the effect on optical signals of different particle sizes can be investigated *a posteriori*, independent of the details of the hydrodynamic or combustion simulation. Additionally, in the efforts reported here, a recently implemented mist temperature floor was explored to improve agreement with observed emissions in Figure 10.

The CTH simulation described in the previous section (Figure 24) provided input to multiple OPTSIG++ simulations using various model parameter choices to represent key emitting materials. As shown above, the CTH simulation reasonably predicts the strong shock and material response of the RP-80 detonator. If the complete optical signal was generated by strong shocks and material response without combustion a CTH-OPTSIG++ prediction should show good agreement with experimental data. The first CTH-OPTSIG++ predictions produced by this effort are shown in Figure 25 and represent a direct implementation of the prior state-of-the-art OPTSIG++ methodology to this problem. Figure 25 compares the relative intensity (W/sr normalized by maximum signal during the initial shock peak) for spatially integrated radiometric signals centered at 575 nm and 850 nm (orange and blue, respectively). The shaded regions represent experimentally observed shot-to-shot variability (see Figure 10), and simulations are provided at 585 nm and 535 nm to visualize predicted signal variability over the relatively wide spectral band. The key takeaways from this simulation are: (1) the timing and relative amplitude (between 575 nm and 850 nm) of the simulated first peak are in good agreement with the data; however, (2) after the 1st peak the simulation and data diverge dramatically.

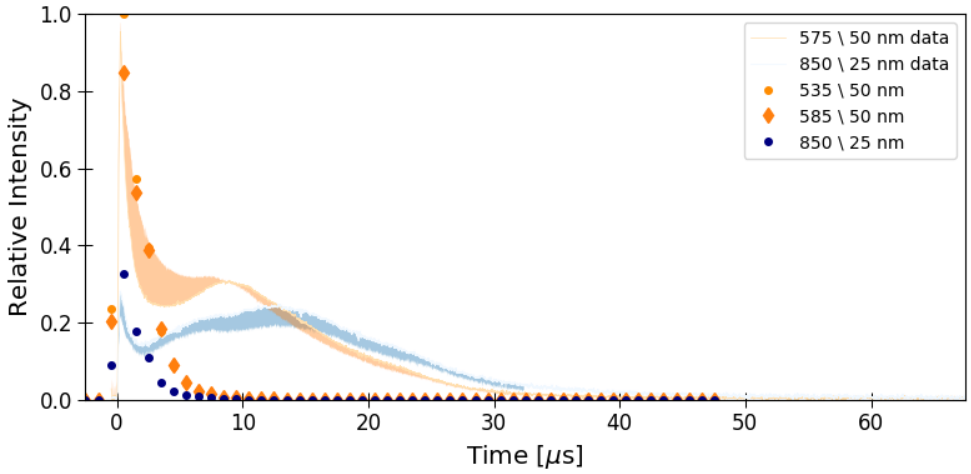

Figure 25: Experimental and simulated optical radiometer data for RP-80 detonator based on the prior state-of-the-art CTH-OPTSIG++ capability (no temperature floor, 10 nm mist particle size, 1.66 g/cm^3 mist particle density).

As discussed in the prior sub-section, CTH does not include gas-phase reactions. Without heat release within the post-detonation fireball, it is postulated that temperatures simulated by CTH decay too quickly thereby underpredicting emissions at later times. To test this hypothesis, the efforts reported here implemented a time-dependent temperature floor in OPTSIG++. As demonstrated in Figure 26, a physically feasible, time-dependent temperature floor for the mist RDX can indeed improve qualitative agreement between the simulated and experimentally observed second emission peak.

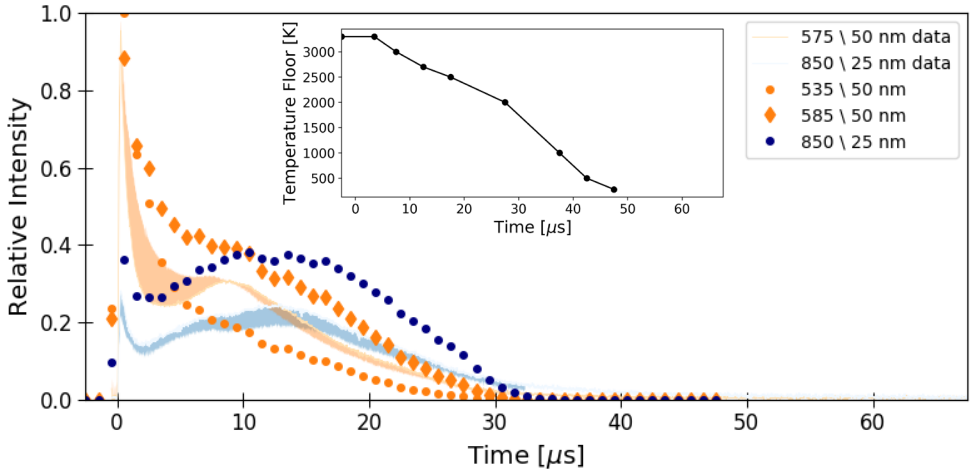

Figure 26: Experimental and simulated optical radiometer data for RP-80 detonator – CTH-OPTSIG++ (time-dependent temperature floor, 10 nm mist particle size, 1.66 g/cc mist particle density).

Next, a literature review [71, 74] led to trying out a $1/\lambda$ soot opacity based on hydrocarbon combustion and pool-fire data, which is experimentally validated near ambient pressure. Applying this model to explosive fireballs is an extrapolation, but one worth exploring, as demonstrated in Figure 27. Figure 27 has the same time-dependent temperature floor as Figure 26. The 850 nm signal is largely unchanged, but the 535 nm and 585 nm signals are significantly different, especially in the creation of the minimum feature between the shock-dominated and combustion-dominated peaks.

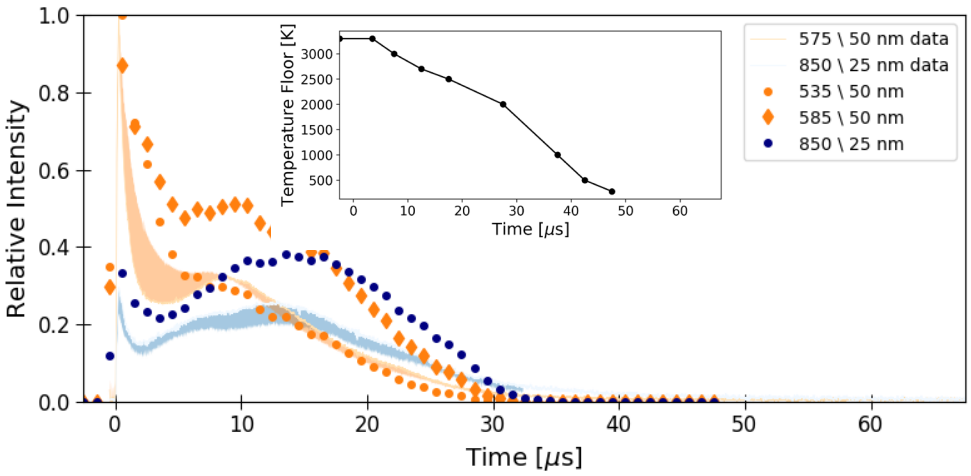

Figure 27: Experimental and simulated optical radiometer data for RP-80 detonator – CTH-OPTSIG++ (time-dependent temperature floor, no mist, Bouguer 1/λ opacity).

Optimizing the time-dependent temperature floor for the continuum Bouguer opacity model leads to a different temperature history than for the mist, as demonstrated in Figure 28. Further modeling (including reactive combustion) and more detailed diagnostic information can potentially determine which optical treatment is most appropriate. Nevertheless, this quick study has helped to map out the sensitivities and modeling degrees of freedom needed to quantitatively validate explosive emission predictions.

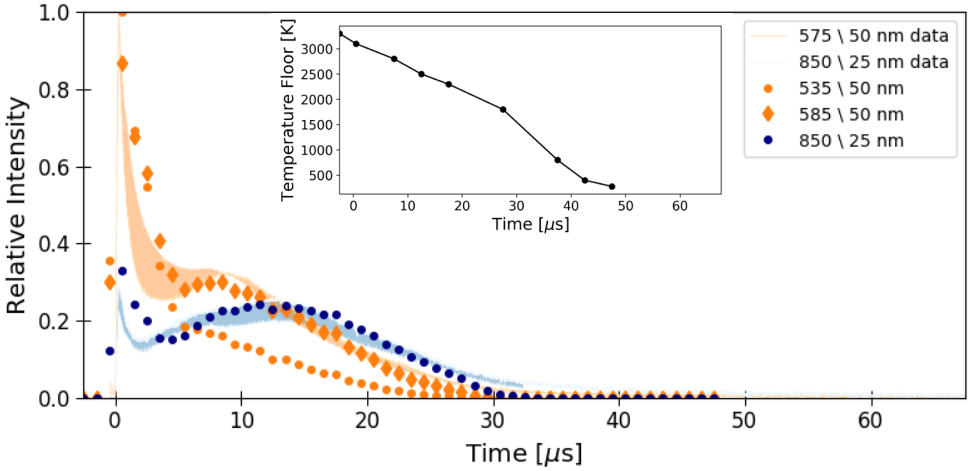

Figure 28: Experimental and simulated optical radiometer data for RP-80 detonator – CTH-OPTSIG++ (time-dependent temperature floor, no mist, Bouguer 1/λ opacity).

3.2.3. HyBurn Reactive LES Predictions

Finally, all simulation results presented thus far are based on the flow field predicted by CTH. As briefly discussed in sub-section 3.2.1, CTH simulations do not include post-detonation reactions and are generally ill-suited for the prediction of turbulence and multi-material mixing. The lack of these phenomena likely contributes to the need for the semi-empirical temperature floor discussed in the prior sub-section on emission models.

As is well established in the literature, fireball phenomena are better predicted by Computational Fluid Dynamics (CFD) simulations using finite rate chemical reactions and formalized multiphase particle models. In a recent example, Kuhl *et al.* [10-12] simulate the post-detonator fireballs from TNT and aluminized explosives using a reactive CFD methodology, including implicit Large Eddy Simulation (LES) of turbulent mixing. In a second example, Houim *et al.* [13-16] have developed a similar LES capability for applications to gas detonations and multiphase coal-dust explosions.

In the current effort, preliminary CFD predictions of the post-detonation fireball from an RP-80 without an aluminum cup were performed by Profs. Houim and Balachandar at University of Florida. For these simulations, an axisymmetric 2D CTH simulation was used to predict detonation within the solid-phase pellets and the initial breakout of the gas-phase blastwave for $t < 4$ μs. At $t = 4$ μs chemical composition was approximated by the equilibrium products of PETN and RDX determined by Sandia's TIGER solver [75] at the temperatures and pressures predicted by CTH. The resulting 2D prediction of gas-phase composition, temperatures, pressures, and velocities at $t = 4$ μs was then used to initialize HyBurn LES predictions.

Figure 29 shows example preliminary results. The top row of Figure 29 shows simulated schlieren images, obtained by post-processing the simulated density field to approximate optical schlieren effects. These simulated schlieren images can be compared with the experimental measurements in the middle row of Figure 9. Next, the middle row of Figure 29 show simulated temperature profiles. These can be compared with the CTH only predictions in Figure 24. Finally, the bottom row of Figure 29 shows the predicted distribution of the OH radical. This is plotted to highlight the fact that the simulations in Figure 29 incorporate gas-phase reactions, which are absent from the CTH only predictions shown in Figure 24

The initial simulations in Figure 29 were 2D, axisymmetric. This was done to minimize computational costs while the research team developed the ability to interface simulations between Sandia's CTH and the University of Florida's HyBurn codes, which was the focus of this effort. In comparison to the fully 3D CTH only predictions shown in Figure 24 the fireball structure observed in Figure 29 does a poorer job matching experimental observations in Figure 9. This is particularly true near the leading tip, where axisymmetric shock collisions likely lead to unrealistic flow phenomena. Future work involving fully 3D HyBurn simulations are expected to address these issues, and ultimately, the HyBurn code will be used to explore the multiphase reactive flow field dynamics of the post-detonation fireball.

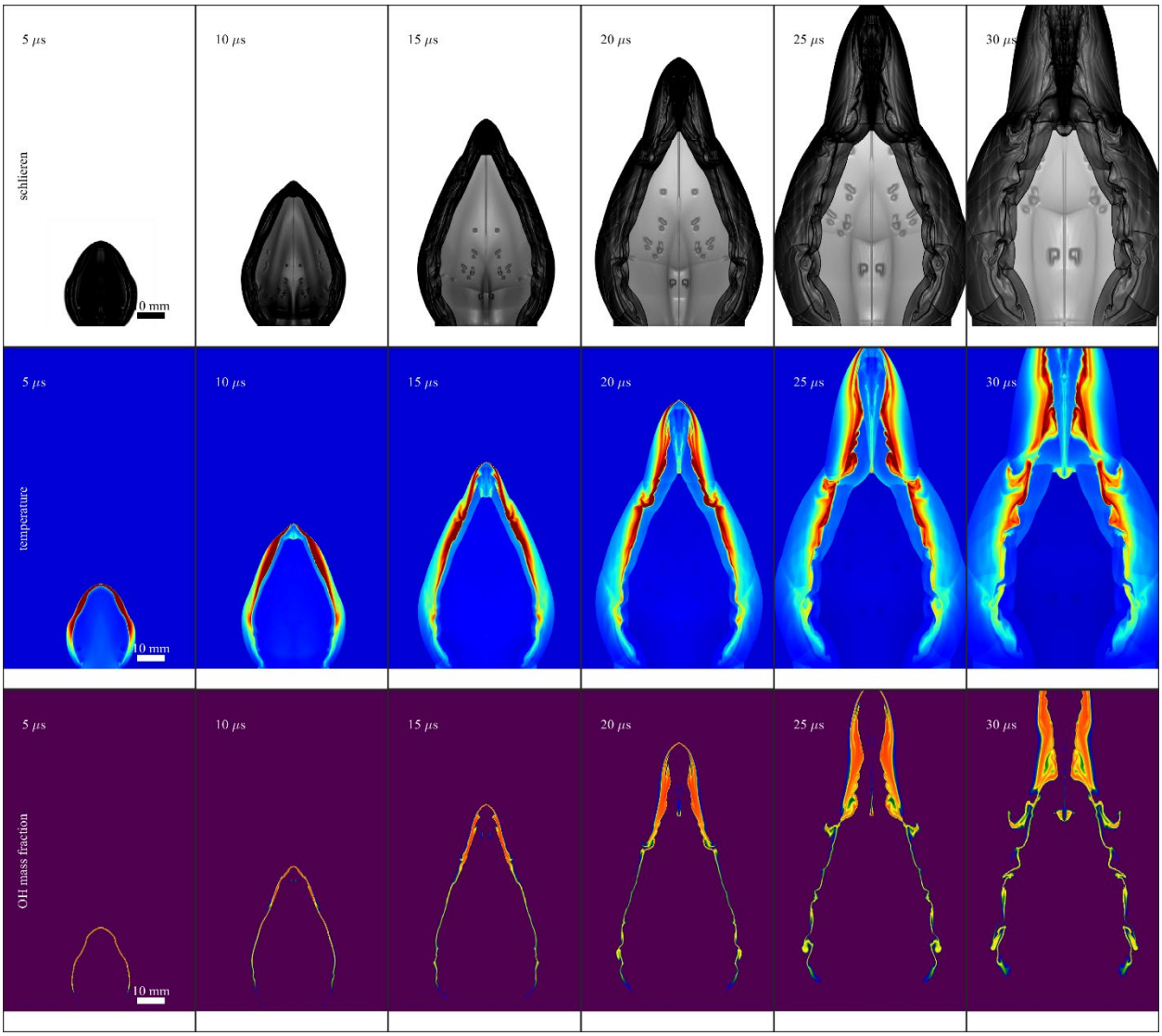

Figure 29: Preliminary 2D axisymmetric HyBurn LES [13-16] predictions of a RP-80 EBW without an aluminum cup. Figure shows simulated schlieren images (top) and contours of temperature (middle) and OH mass fraction (bottom) for fields of view corresponding to the experimental images in Figure 9.

This page left blank

4. CONCLUSIONS AND FUTURE WORK

Following the detonation of large-scale explosive devices, the fragmentation of metallic components and generation of hot, luminous fireballs result in extreme hazards that greatly complicate scientific measurement of post-detonation environments. This report briefly summarizes findings from a Laboratory Directed Research and Development (LDRD) effort at Sandia National Laboratories, which postulated that scientific developments could be accelerated with experimental testing at greatly reduced scales. Here, commercially purchased, gram-scale explosive devices are shown to enable improved imaging and laser diagnostics for explosive fragmentation and post-detonation fireballs. Measurements results are presented along with preliminary simulations of these phenomena. Significant developments are highlighted below with more details available in several publications that resulted from these efforts [17-25].

- Commercially purchased and customized exploding bridgewire (EBW) detonators containing less than a gram of explosives are shown to fragment and produce luminous post-detonation fireballs that mimic phenomena commonly observed in much larger scale device testing. In addition, per-shot costs of EBW detonators are orders of magnitude less than typical large-scale device testing. As demonstrated here, these advantages accelerate opportunities for diagnostic advancement and experimental repetition.

- Digital Image Correlation (DIC) and optical fragment tracking were extended for MHz quantification of the deformation and fragmentation of the metallic case. Compared to prior applications of these diagnostics at larger-scale, experiments reported here allow for significant repetition, enabling quantification of experimental uncertainties.

- Diagnostics for post-detonation fireballs have been extended with non-intrusive laser measures of temperatures and particulates based on Coherent Anti-Stokes Raman Scattering (CARS) and Laser Induced Incandescence (LII), respectively. Furthermore, reduced experimental hazards and per-shot costs, enabled several other experimental diagnostics. Taken together, measurement results presented here may be the most complete dataset of a post-detonation fireball, albeit at reduced experimental scales compared to many applications.

- Initial simulation results show that models primarily developed for large-scale applications can predict phenomena observed in the reduced-scale experiments. As demonstrated by a few examples, the extensive experimental datasets provided by this work enable new opportunities for model validation.

Future work is planned to continue diagnostic and model developments through benchtop scale experiments. In addition, several efforts at Sandia National Laboratories are now incorporating lessons learned from the current project into applications at much larger scales.

REFERENCES

[1] Cooper, P. W., 2018, Explosives engineering, John Wiley & Sons.

[2] Gold, V. M. and Baker, E. L., 2008, "A model for fracture of explosively driven metal shells," Engineering Fracture Mechanics, 75(2), pp. 275-289.

[3] Goto, D. M., Becker, R., Orzechowski, T. J., Springer, H. K., Sunwoo, A. J. and Syn, C. K., 2008, "Investigation of the fracture and fragmentation of explosively driven rings and cylinders," International Journal of Impact Engineering, 35(12), pp. 1547-1556.

[4] Hiroe, T., Fujiwara, K., Hata, H. and Takahashi, H., 2008, "Deformation and fragmentation behaviour of exploded metal cylinders and the effects of wall materials, configuration, explosive energy and initiated locations," International Journal of Impact Engineering, 35(12), pp. 1578-1586.

[5] Li, B., Pandolfi, A. and Ortiz, M., 2015, "Material-point erosion simulation of dynamic fragmentation of metals," Mech. Mater., 80, pp. 288-297.

[6] Olovsson, L., Limido, J., Lacome, J.-L., Hanssen, A. G. and Petit, J., 2015, "Modeling fragmentation with new high order finite element technology and node splitting," EPJ Web of Conferences, 94, p. 04050.

[7] Gullerud, A. and Hollenshead, J., 2017, "Coupled Euler-Lagrange simulations of metal fragmentation in pipe bomb configurations," Procedia Engineering, 204, pp. 202-207.

[8] Liu, M., Ren, G., Fan, C., Tang, T., Wang, X. and Hu, H., 2017, "Experimental and numerical studies on the expanding fracture behavior of an explosively driven 1045 steel cylinder," International Journal of Impact Engineering, 109, pp. 240-252.

[9] Rasico, J. G., Newman, C. A. and Jensen, M. R., 2018, "Modelling fragmentation of a 155 mm artillery shell IED in a buried mine blast event," International Journal of Vehicle Performance, 4(4), pp. 323-346.

[10] Grote, D., Kuhl, A. L., Bell, J. B. and Beckner, V. E., 2015, "Modeling Optical Emissions from HE Fireballs," Proc. 25th International Colloquium on the Dynamics of Explosions and Reactive Systems (ICDERS).

[11] Kuhl, A. L. and Balakrishnan, K., 2012, "Gasdynamic model of dilute two-phase combustion fields," Combustion, Explosion, and Shock Waves, 48(5), pp. 544-560.

[12] Kuhl, A. L., Bell, J. B., Beckner, V. E. and Reichenbach, H., 2011, "Gasdynamic model of turbulent combustion in TNT explosions," Proceedings of the Combustion Institute, 33(2), pp. 2177-2185.

[13] Houim, R. W. and Taylor, B. D., 2019, "Detonation initiation from shock and material interface interactions in hydrogen-air mixtures," Proceedings of the Combustion Institute, 37(3), pp. 3513-3520.

[14] Lai, S., Houim, R. W. and Oran, E. S., 2018, "Effects of particle size and density on dust dispersion behind a moving shock," Physical Review Fluids, 3(6), p. 064306.

[15] Houim, R. W. and Oran, E. S., 2016, "A multiphase model for compressible granular–gaseous flows: formulation and initial tests," J. Fluid Mech., 789, pp. 166-220.

[16] Houim, R. W. and Oran, E. S., 2015, "Numerical simulation of dilute and dense layered coal-dust explosions," Proceedings of the Combustion Institute, 35(2), pp. 2083-2090.

[17] Guildenbecher, D., Jones, E. M. C., Hall, E. M., Reu, P. L., Miller, T. J., Perez, F., Thompson, A. D. and Ball, J. P., 2021, "Imaging Diagnostics and Simulations of Metal Fragmentation from Gram-Scale Explosive Devices," In Preparation.

[18] Richardson, D. R., Kearney, S. P. and Guildenbecher, D., 2020, "Three-Beam Rotational Coherent Anti-Stokes Raman Spectroscopy (CARS) Thermometry in Scattering Environments," Applied Optics, Accepted for Publication.

[19] Richardson, D., Kearney, S. and Guildenbecher, D., 2020, "Post-Detonation Fireball Thermometry via Femtosecond-Picosecond Coherent Anti-Stokes Raman Scattering (CARS)," Proceedings of the Combustion Institute, Accepted for Presentation.

[20] Brown, A., Son, S., Meyer, T. and Guildenbecher, D., 2020, "Emission diagnostics for benchtop-scale explosive fireballs," Proc. Laser Applications to Chemical, Security and Environmental Analysis.

[21] Halls, B. R., Quintana, E., Lebow, L. and Guildenbecher, D. R., 2019, "High-Speed Fragment Tracking with X-ray Radiography," Proc. AIAA Scitech 2019 Forum, p. 0271.

[22] Halls, B. R., 2019, "Preliminary Investigation of Apparent Mass Loss in Objects Due to Image Blur using X-ray Radiography," Proc. ILASS-Americas 30th Annual Conference on Liquid Atomization and Spray Systems.

[23] Guildenbecher, D., Olles, J. D., Miller, T. J., Reu, P. L., Yeager, J. D., Bowden, P. R. and Schmalzer, A. M., 2018, "Characterization of hypervelocity fragments and subsequent HE initiation," Proc. International Detonation Symposium.

[24] White, C., Orth, M., Gabl, J. R., Whitehead, B. E. and Pourpoint, T. L., 2020, "High Speed Diagnostics using Chemiluminescence Thermometry in a Shock Tube," AIAA Propulsion and Energy 2020 Forum.

[25] Chen, Y., Cenker, E., Richardson, D. R., Kearney, S. P., Halls, B. R., Skeen, S. A., Shaddix, C. R. and Guildenbecher, D. R., 2018, "Single-camera, single-shot, time-resolved laser-induced incandescence decay imaging," Opt. Lett., 43(21), pp. 5363-5366.

[26] Teledyne RISI, 2020, "RP-80 EBW Detonator," http://www.teledynerisi.com/products-services/ebw-detonators/rp-80-ebw-detonator.

[27] Rae, P. J. and Dickson, P. M., 2019, "A review of the mechanism by which exploding bridge-wire detonators function," Proceedings of the Royal Society A: Mathematical, Physical and Engineering Sciences, 475(2227), p. 20190120.

[28] Smilowitz, L., Henson, B., Remelius, D., Suvorova, N., Oschwald, D. and Thomas, K., 2018, "Measurements of observables during detonator function," AIP Conference Proceedings, 1979(1), p. 150035.

[29] Smilowitz, L., Remelius, D., Suvorova, N., Bowlan, P., Oschwald, D. and Henson, B. F., 2019, "Finding the "lost-time" in detonator function," Appl. Phys. Lett., 114(10), p. 104102.

[30] Monat, J. E., Carney, J. R. and Pangilinan, G. I., 2004, "Novel Optical Fiber-Based Gauge for Measuring Transient Pressures," AIP Conference Proceedings, 706(1), pp. 1281-1284.

[31]Granholm, R. H. and Sandusky, H. W., 2006, "Small-Scale Shock Reactivity and Internal Blast Test," AIP Conference Proceedings, 845(1), pp. 1257-1260.

[32]Fouchier, C., Laboureur, D., Youinou, L., Lapebie, E. and Buchlin, J. M., 2017, "Experimental investigation of blast wave propagation in an urban environment," Journal of Loss Prevention in the Process Industries, 49, pp. 248-265.

[33]Teledyne RISI, 2020, "FS-43 Firing System," http://www.teledynerisi.com/products-services/fire-sets/fs-43-firing-system.

[34]Ren, G., Guo, Z., Fan, C., Tang, T. and Hu, H., 2016, "Dynamic shear fracture of an explosively-driven metal cylindrical shell," International Journal of Impact Engineering, 95, pp. 35-39.

[35]Wang, X. y., Wang, S. S. and Ma, F., 2018, "Experimental study on the expansion of metal cylinders by detonation," International Journal of Impact Engineering, 114, pp. 147-152.

[36]Bors, D., Cummins, J. and Goodpaster, J., 2014, "The Anatomy of a Pipe Bomb Explosion: Measuring the Mass and Velocity Distributions of Container Fragments," Journal of Forensic Sciences, 59(1), pp. 42-51.

[37]Huang, G.-y., Li, W. and Feng, S.-s., 2015, "Axial distribution of Fragment Velocities from cylindrical casing under explosive loading," International Journal of Impact Engineering, 76, pp. 20-27.

[38]Guo, Z.-w., Huang, G.-y., Liu, C.-m. and Feng, S.-s., 2018, "Velocity axial distribution of fragments from non-cylindrical symmetry explosive-filled casing," International Journal of Impact Engineering, 118, pp. 1-10.

[39]Oxley, J. C., Smith, J. L., Bernier, E. T., Sandstrom, F., Weiss, G. G., Recht, G. W. and Schatzer, D., 2018, "Characterizing the Performance of Pipe Bombs," Journal of Forensic Sciences, 63(1), pp. 86-101.

[40]Reu, P. L., 2012, "Introduction to Digital Image Correlation: Best Practices and Applications," Experimental Techniques, 36(1), pp. 3-4.

[41]Curry, R. J. and Langdon, G. S., 2017, "Transient response of steel plates subjected to close proximity explosive detonations in air," International Journal of Impact Engineering, 102, pp. 102-116.

[42]Cooper, M. A., Reu, P. L. and Miller, T. J., 2010, "Observations in Explosive Systems with High-Speed Digital Image Correlation," Proc. 14th International Detonation Symposium.

[43]Rigby, S., Tyas, A., Curry, R. and Langdon, G., 2019, "Experimental measurement of specific impulse distribution and transient deformation of plates subjected to near-field explosive blasts," Experimental Mechanics, 59(2), pp. 163-178.

[44]Chen, P. W., Liu, H., Ding, Y. S., Guo, B. Q., Chen, J. J. and Liu, H. B., 2016, "Dynamic Deformation of Clamped Circular Plates Subjected to Confined Blast Loading," Strain, 52(6), pp. 478-491.

[45]Oxley, J., Smith, J., Resende, E., Rogers, E., Strobel, R. and Bender, E., 2001, "Improvised Explosive Devices: Pipe Bombs," Journal of Forensic Sciences, 46(3), pp. 510-534.

[46]Zhang, Z., Huang, F., Cao, Y. and Yan, C., 2018, "A fragments mass distribution scaling relations for fragmenting shells with variable thickness subjected to internal explosive loading," International Journal of Impact Engineering, 120, pp. 79-94.

[47]da Silva, L. A., Johnson, S., Critchley, R., Clements, J., Norris, K. and Stennett, C., 2020, "Experimental fragmentation of pipe bombs with varying case thickness," Forensic Science International, 306, p. 110034.

[48]Gregory, O., Oxley, J., Smith, J., Platek, M., Ghonem, H., Bernier, E., Downey, M. and Cumminskey, C., 2010, "Microstructural characterization of pipe bomb fragments," Mater. Charact., 61(3), pp. 347-354.

[49]Liang, M., Li, X. and Lu, F., 2017, "Modeling the dynamic fracture and fragmentation of explosive-driven metal ring with notches or grooves," Archive of Applied Mechanics, 87(4), pp. 617-631.

[50]Guildenbecher, D. R., Cooper, M. A. and Sojka, P. E., 2016, "High-speed (20 kHz) digital in-line holography for transient particle tracking and sizing in multiphase flows," Applied Optics, 55(11), pp. 2892-2903.

[51]Taylor, G. I., 1963, Scientific Papers of Sir Geoffrey Ingram Taylor: Volume III Aerodynamics and the Mechanics of Projectiles and Explosions, Cambridge at the University Press.

[52]Hoggatt, C. R. and Recht, R. F., 1968, "Fracture Behavior of Tubular Bombs," J. Appl. Phys., 39(3), pp. 1856-1862.

[53]RISI, T., 2020, "RP-1 EBW Detonator," https://www.teledynedefenseelectronics.com/energetics/products/Pages/EBW%20Detonators.aspx#RP-1.

[54]Lebel, L. S., Brousseau, P., Erhardt, L. and Andrews, W. S., 2014, "Thermochemistry of the combustion of gas phase and condensed phase detonation products in an explosive fireball," Combust. Flame, 161(4), pp. 1038-1047.

[55]Gordon, J. M., Spidell, M. T., Pitz, J., Gross, K. C. and Perram, G. P., 2010, High speed spectral measurements of IED detonation fireballs, SPIE.

[56]Gordon, J. M., Gross, K. C. and Perram, G. P., 2009, Temporally resolved infrared spectra from the detonation of advanced munitions, SPIE.

[57]Gordon, J. M., Gross, K. C. and Perram, G. P., 2013, Temperature dynamics of aluminized cyclotrimethylenetrinitramine fireballs for event classification, SPIE.

[58]Lebel, L. S., Brousseau, P., Erhardt, L. and Andrews, W. S., 2013, "Measurements of the Temperature Inside an Explosive Fireball," Journal of Applied Mechanics, 80(3), pp. 031702-031702-031706.

[59]Settles, G. S., 2006, Schlieren and shadowgraph techniques: Visualizing phenomena in transparent media, Springer-Verlag, Berlin.

[60]Hargather, M. J. and Settles, G. S., 2007, "Optical measurement and scaling of blasts from gram-range explosive charges," Shock Waves, 17(4), pp. 215-223.

[61]Lewis, W. K. and Rumchik, C. G., 2009, "Measurement of apparent temperature in post-detonation fireballs using atomic emission spectroscopy," J. Appl. Phys., 105(5), p. 056104.

[62] Lewis, W. K., Rumchik, C. G., Broughton, P. B. and Lindsay, C. M., 2012, "Time-resolved spectroscopic studies of aluminized explosives: Chemical dynamics and apparent temperatures," J. Appl. Phys., 111(1), p. 014903.

[63] Abdul-Karim, N., Blackman, C. S., Gill, P. P., Morgan, R. M., Matjacic, L., Webb, R. and Ng, W. H., 2016, "Morphological Variations of Explosive Residue Particles and Implications for Understanding Detonation Mechanisms," Anal. Chem., 88(7), pp. 3899-3908.

[64] Abdul-Karim, N., Blackman, C. S., Gill, P. P. and Karu, K., 2016, "The spatial distribution patterns of condensed phase post-blast explosive residues formed during detonation," J. Hazard. Mater., 316, pp. 204-213.

[65] Pantea, D., Brochu, S., Thiboutot, S., Ampleman, G. and Scholz, G., 2006, "A morphological investigation of soot produced by the detonation of munitions," Chemosphere, 65(5), pp. 821-831.

[66] Gross, K. C., Wayman, J. and Perram, G. P., 2007, Phenomenological fireball model for remote identification of high-explosives, SPIE.

[67] Gross, K. C., Perram, G. P. and Tuttle, R. F., 2005, Modeling infrared spectral intensity data from bomb detonations, SPIE.

[68] Gross, K. C., Dills, A. M., Perram, G. P. and Tuttle, R. F., 2003, Phenomenology of exploding ordnance using spectrally and temporally resolved infrared emissions, SPIE.

[69] Michelsen, H. A., Schulz, C., Smallwood, G. J. and Will, S., 2015, "Laser-induced incandescence: Particulate diagnostics for combustion, atmospheric, and industrial applications," Prog. Energy Combust. Sci., 51, pp. 2-48.

[70] Schulz, C., Kock, B. F., Hofmann, M., Michelsen, H., Will, S., Bougie, B., Suntz, R. and Smallwood, G., 2006, "Laser-induced incandescence: recent trends and current questions," Appl. Phys. B, 83(3), p. 333.

[71] Williams, T. C., Shaddix, C. R., Jensen, K. A. and Suo-Anttila, J. M., 2007, "Measurement of the dimensionless extinction coefficient of soot within laminar diffusion flames," Int. J. Heat Mass Transfer, 50(7), pp. 1616-1630.

[72] Smyth, K. C. and Shaddix, C. R., 1996, "The elusive history of m~= 1.57 – 0.56i for the refractive index of soot," Combust. Flame, 107(3), pp. 314-320.

[73] Hertel, E., Bell, R., Elrick, M., Farnsworth, A., Kerley, G., McGlaun, J., Petney, S., Silling, S., Taylor, P. and Yarrington, L., 1995, "CTH: A software family for multi-dimensional shock physics analysis," Shock Waves@ Marseille I, Springer, pp. 377-382.

[74] Jensen, K. A., Suo-Anttila, J. M. and Blevins, L. G., 2007, "Measurement of soot morphology, chemistry, and optical properties in the visible and near-infrared spectrum in the flame zone and overfire region of large JP-8 pool fires," Combust. Sci. Technol., 179(12), pp. 2453-2487.

[75] Hobbs, M., 2017, "CTH-TIGER tutorial (thermochemical equilibrium code distributed with CTH)," SAND2017-5606PE, Sandia National Laboratories, Albuquerque, New Mexico.

APPENDIX A. DETONATION DRIVEN SHOCK TUBE FOR FIREBALL GENERATION

The main report summarizes diagnostic and simulation developments for study of post-detonation fireballs produced by commercial detonators with less than a gram of explosive. As discussed there, this experimental platform is advantageous due to reduced hazards and per-shot costs compared to much larger-scale explosive device applications. However, as also observed in the discussion above, even at the benchtop scale, explosive experiments produce multi-phase flows whose detailed chemical processes are not always well-understood and are difficult to measure.

Here, an alternative experimental platform based on a gas-phase, detonation driven shock tube is discussed. Work reported here was performed at Purdue University and supported by Sandia's Academic Alliance Laboratory Directed Research and Development Program (LDRD). As discussed further below, the goal of the LDRD efforts at Purdue was to develop an alternative experimental facility for study of turbulent, reacting fireballs, which complements and expands the capabilities developed by the efforts discussed in the main report above.

As shown here, and in a more detailed publication [24], an open-ended detonation driven shock tube produces a turbulent fireball akin to that from the detonation of high explosives discussed in the main report. However, in contrast to explosive devices, the shock tube developed here also allows for precise control and variation of reactants. Furthermore, with the use of a few select reactant species, such as the hydrogen-oxygen experiments demonstrated here, it is possible to create fireballs with well-studied reaction mechanisms. As such, a shock tube may be an effective alternative platform for diagnostic and model development.

The detonation driven shock tube developed for this study currently uses hydrogen and oxygen as the driving gases and is shown schematically in Figure A-1 with a photo of the flow conditioning configuration shown in Figure A-2. The shock tube is sealed with a burst disk installed in between two CF flanges. Early testing reported in [24] used a burst disk made of HDPE film. However, results reported in [24] indicate that the HPDE film likely mixes with and alters the resulting fireball. Here, additional results are reported utilizing a brass burst disk. As shown in the experimental images of the resulting fireball in Figure A-3, testing with this brass burst disk produces what appears to be a cleaner fireball with blue/green emission, as generally expected for a hydrogen-oxygen flame.

Many more details on the development of this facility are reported in [24]. Overall, the advancements reported here demonstrate successful construction and initial operation of a unique detonation driven shock tube. Future work will extend and expand the diagnostics discussed in the main report for quantitative measures of the gas-phase fireballs exemplified in Figure A-3.

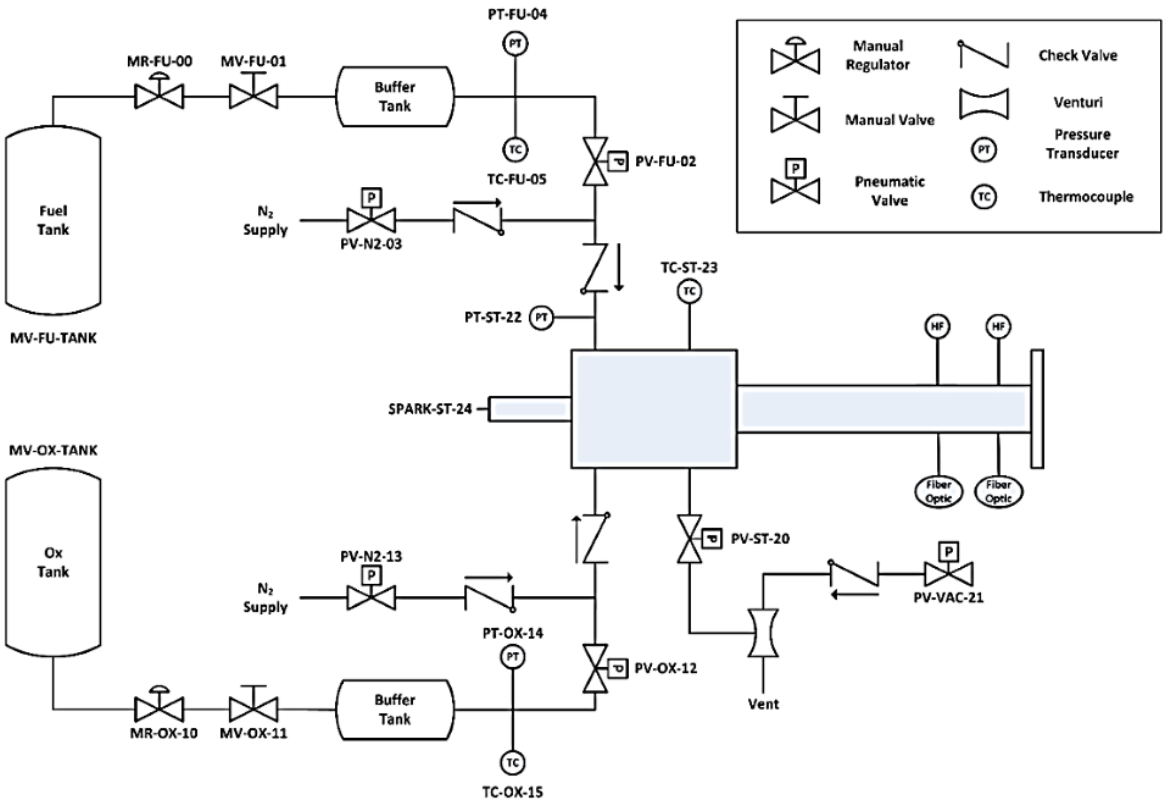

Figure A-1. Pluming and instrumentation diagram for the detonation driven shock tube developed here.

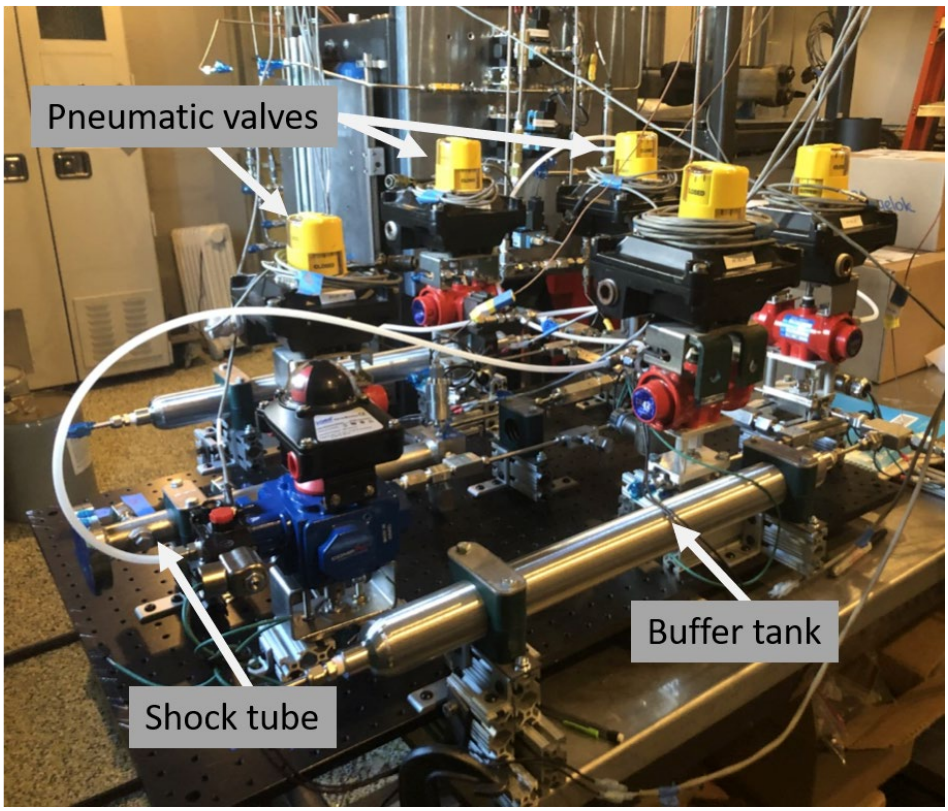

Figure A-2. Photo of the shock tube facility highlighting the flow conditioning configuration.

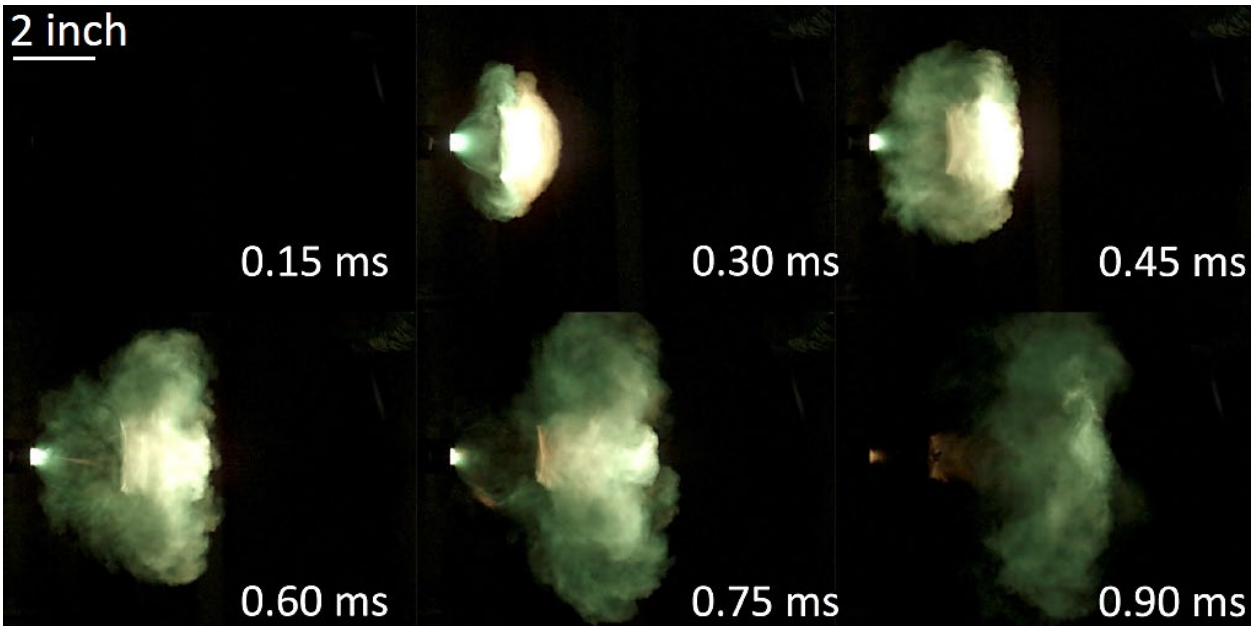

Figure A-3. Experimental images of the fireball emitted from the open end of the shock tube fed by a hydrogen-oxygen mixture.

This page left blank

DISTRIBUTION

Email—Internal

Name	Org.	Sandia Email Address
Elise M. Hall	1512	emhall2@sandia.gov
Benjamin R. Halls	1512	brhalls@sandia.gov
Elizabeth M.C. Jones	1512	emjones@sandia.gov
Sean P. Kearney	1512	spkearn@sandia.gov
Phillip L. Reu	1512	plreu@sandia.gov
Ryan T. Marinis	2554	rtmarin@sandia.gov
Francisco Perez	6623	frapere@sandia.gov
Andrew D. Thompson	6626	andthom@sandia.gov
Christopher Murzyn	6751	cmurzyn@sandia.gov
Ann R. Dallman	6775	ardallm@sandia.gov
Marc C. Welliver	6775	mwelliv@sandia.gov
Technical Library	01977	sanddocs@sandia.gov

Email—External

Name	Company Email Address	Company Name
S. Balachandar	bala1s@ufl.edu	University of Florida
Alex D. Brown	brow1537@purdue.edu	Purdue University
Ryan W. Houim	rhouim@ufl.edu	University of Florida
Ellen Chen Mazumdar	ellen.mazumdar@gatech.edu	Georgia Tech
Timothee L. Pourpoint	timothee@purdue.edu	Purdue University
Catriona M. L. White	white444@purdue.edu	Purdue University

This page left blank

This page left blank

Sandia National Laboratories

Sandia National Laboratories is a multimission laboratory managed and operated by National Technology & Engineering Solutions of Sandia LLC, a wholly owned subsidiary of Honeywell International Inc. for the U.S. Department of Energy's National Nuclear Security Administration under contract DE-NA0003525.